Monthly Notices of the ROYAL ASTRONOMICAL SOCIETY

MNRAS **500,** 3290–3308 (2021) doi:10.1093/mnras/staa3384
Advance Access publication 2020 October 31

Turbulent dissipation, CH^+ abundance, H_2 line luminosities, and polarization in the cold neutral medium

Eric R. Moseley [1]★ B. T. Draine,[1] Kengo Tomida[2] and James M. Stone[1,3]

[1]*Department of Astrophysical Sciences, Princeton University, Princeton, NJ 08540, USA*
[2]*Astronomical Institute, Tohoku University, Sendai, Miyagi 980-8578, Japan*
[3]*School of Natural Sciences, Institute for Advanced Study, Princeton, NJ 08544, USA*

Accepted 2020 October 21. Received 2020 September 21; in original form 2020 June 6

ABSTRACT

In the cold neutral medium, high out-of-equilibrium temperatures are created by intermittent dissipation processes, including shocks, viscous heating, and ambipolar diffusion. The high-temperature excursions are thought to explain the enhanced abundance of CH^+ observed along diffuse molecular sightlines. Intermittent high temperatures should also have an impact on H_2 line luminosities. We carry out simulations of magnetohydrodynamic (MHD) turbulence in molecular clouds including heating and cooling, and post-process them to study H_2 line emission and hot-gas chemistry, particularly the formation of CH^+. We explore multiple magnetic field strengths and equations of state. We use a new H_2 cooling function for $n_H \leq 10^5\,cm^{-3}$, $T \leq 5000\,K$, and variable H_2 fraction. We make two important simplifying assumptions: (i) the H_2/H fraction is fixed everywhere and (ii) we exclude from our analysis regions where the ion–neutral drift velocity is calculated to be greater than 5 km s^{-1}. Our models produce H_2 emission lines in accord with many observations, although extra excitation mechanisms are required in some clouds. For realistic root-mean-square (rms) magnetic field strengths ($\approx$10 μG) and velocity dispersions, we reproduce observed CH^+ abundances. These findings contrast with those of Valdivia et al. (2017) Comparison of predicted dust polarization with observations by *Planck* suggests that the mean field is $\gtrsim$5 μG, so that the turbulence is sub-Alfvénic. We recommend future work treating ions and neutrals as separate fluids to more accurately capture the effects of ambipolar diffusion on CH^+ abundance.

Key words: astrochemistry – polarization – turbulence – ISM: abundances – ISM: clouds – ISM: magnetic fields.

1 INTRODUCTION

The abundance of CH^+ in diffuse interstellar clouds has been a challenge to explain since it was first identified (Douglas & Herzberg 1941). The observed column densities ($\gtrsim 10^{13}\,cm^{-2}$; Lambert & Danks 1986) are puzzling due to the multiple efficient destruction mechanisms for CH^+: reactions with H, H_2, e^-, and dissociation by ultraviolet radiation. In addition, the reaction

$$C^+ + H_2 \rightarrow CH^+ + H \qquad \Delta E/k = 4640\ K \qquad (1)$$

is strongly endothermic and only proceeds appreciably for temperatures $T \gtrsim 1000\,K$, significantly higher than the $\sim 100\,K$ temperatures characteristic of these clouds. As a result, steady-state models fail to produce CH^+ in sufficient quantities, predicting column densities at least two orders of magnitude below observed values (van Dishoeck & Black 1986).

Proposed solutions to this problem rely on ways to heat some fraction of the gas, even transiently, to $T \gtrsim 1000\,K$. Elitzur & Watson (1978) proposed that shock waves in diffuse molecular clouds could account for the CH^+ production, and two-fluid magnetohydrodynamic (MHD) shock models were subsequently used to model CH^+ formation (Flower, Pineau des Forets & Hartquist 1985; Draine 1986b; Draine & Katz 1986a,b). Other solutions have also been proposed, including diffuse gas undergoing strong photoelectric heating (White 1984), dense photon-dominated regions (PDRs; Duley et al. 1992; Sternberg & Dalgarno 1995), and heating in boundary layers at cloud surfaces (Duley et al. 1992).

As diffuse interstellar clouds are supersonically turbulent, intermittent shock heating is one possible way to heat enough of the gas to these temperatures. On the basis of laboratory experiments of turbulent flows, Falgarone & Puget (1995) suggested that intermittent dissipation of turbulence could heat diffuse molecular clouds to these temperatures. Pan & Padoan (2009) found that, in compressible MHD turbulence simulations, a few per cent of the gas by mass could be heated to $\gtrsim 1000\,K$ in such diffuse molecular clouds, and thus produce the observed amounts of CH^+. These findings may also help to explain observed levels of H_2 rotational line emission (e.g. Ingalls et al. 2011) as well. High-j states of H_2 can only be effectively populated in relatively hot gas ($\gtrsim$ 1000K) or through ultraviolet pumping. It is thus not surprising that CH^+ column density and rotationally excited H_2 are correlated (Frisch & Jura 1980; Lambert & Danks 1986).

Drift between ionic and neutral species in MHD shocks has been proposed as a way to help overcome the energy barrier in reaction (1) (Draine 1980; Flower et al. 1985). Myers, McKee & Li (2015, hereafter MML15) analysed MHD turbulence simulations with an isothermal equation of state for the purpose of addressing the CH^+

★ E-mail: moseley@princeton.edu

abundance and found that the contribution to the reaction rate from ion–neutral drift was the dominant effect responsible for generating CH^+.

In disagreement with the results of MML15 are those of Valdivia et al. (2017, hereafter V17). V17 ran a two-phase, colliding flow MHD simulation and found that CH^+ was *not* primarily produced by high ion–neutral drift velocities in their simulations. Their simulations also underproduced CH^+ relative to observations, for reasons that they discuss. For one, it seems that the ion–neutral drift velocity distribution is not converged, and these velocities increase in magnitude at higher resolution. Secondly, due to the nature of colliding flow simulations that inject a single, warm phase of interstellar mass (ISM) into the box, they likely underestimate the H_2 fraction in low-density regions. In addition, highly excited H_2 may help to overcome the high reaction barrier present in reaction (1).

Our approach bears more similarity to that of MML15. Like MML15, we have run ideal MHD turbulence simulations to understand the abundance of CH^+. We use the same abundances of H, H_2, e^-, C, and O, the same mean density, and the same box size to make our simulations as directly comparable to theirs as possible. Two of our simulations use a low initial magnetic field strength (0.5 μG), and two use a high magnetic field strength (4.5 μG). Two are run with an isothermal equation of state as in MML15, and two are run with an adiabatic ($\gamma = 5/3$) equation of state with heating and cooling processes included throughout the simulation. For all of our simulations, we also estimate the ambipolar diffusion heating in each cell with a post-processing scheme described in Section 3.3. This effect is separate from the streaming-induced enhancement of the reaction rate, and similarly important. In our simulations, the ambipolar diffusion heating rate can become the dominant heating term in the low-density regions where MML15 determined the majority of CH^+ is produced. We present maps of total column density and H_2 rotational line intensities for those simulations that include heating and cooling processes throughout in Fig. 1.

Because turbulence leads to disorder in the magnetic field, we check to see whether the proposed levels of MHD turbulence are consistent with observations of polarized emission from aligned dust grains (Planck Collaboration XXI 2015c; Planck Collaboration XII 2020).

In Section 2, we review our model, the effects of ambipolar diffusion, and the relevant heating processes. In Section 4, we detail our (new) calculation for the H_2 cooling function and an accurate fit to it for computational ease (see also Appendix B), as well as describe the C^+ and O line cooling that we use. In Section 4.2, we discuss details of H_2 line emission. Then, in Section 5, we describe the chemistry that goes into producing CH^+. We present our results for the temperature and drift velocity in our simulations, the CH^+ abundance, the velocity distributions of CH^+ molecules, H_2 rotational line emission, and the polarization of dust emission in Section 6. Finally, we discuss our results in Section 7 and provide a summary of our findings in Section 8. A summary of our simulation parameters and results can be found in Tables 1 and 2, respectively.

2 FLUID DYNAMICS

As described in Section 1, our simulations are designed to study the formation of the CH^+ molecule and emission from H_2 rotational transitions in turbulent molecular clouds.

To investigate the importance of magnetic field strength, and to compare different treatments of the fluid dynamics, we have run a number of simulations. In Appendix A, we explore the numerical convergence of our results using resolutions ranging from 64^3 through 512^3. In the body of this paper; however, we will focus on simulations run at a resolution of 512^3.

For each magnetic field strength, we calculate the fluid motions assuming ideal MHD and explicit heating and cooling. We also carry out simulations using ideal MHD and an isothermal equation of state, to evaluate the effects of heating and cooling on the fluid motions. We post-process these isothermal simulations following a procedure similar to that given in MML15 (see Section 3). Our post-processing of the isothermal simulations differs from MML15 in that we use a new H_2 cooling function (equation 17), and we attempt to estimate the effects of ambipolar diffusion heating on the system as described in the coming sections.

2.1 Models and scaling

Intermittent dissipation events in molecular clouds arise from the supersonic MHD turbulence that pervades them. To model these clouds, we use the results of four 512^3 driven MHD turbulence simulations run with the astrophysical MHD code ATHENA++.[1] These simulations utilize periodic boundary conditions and a cubic domain. They are driven solenoidally between wavenumbers $k = 2\pi/\ell_0, 4\pi/\ell_0$ with a power spectrum $P(k) \propto k^{-2}$, where $\ell_0 = 20$ pc is the length of a side of the simulation volume. The driving follows the Ornstein–Uhlenbeck process (Lynn et al. 2012), smoothly evolving the driving with a correlation time of about 1/10 of a dynamical time. We use the Harten–Lax–van Leer-Discontinuities (HLLD) Riemann solver together with a second-order Piecewise-Linear-Mesh (PLM) primitive reconstruction with a second-order van Leer time integrator. As magnetic fields and their effects in molecular clouds may vary, we use two initial field strengths to compare to one another: 0.5 and 4.5 μG.

Simulations begin with a uniform medium and uniform magnetic field $\boldsymbol{B}_0$, and are then driven until the velocity dispersion σ_{3D} and the rms magnetic field strength $B_{\rm rms}$ saturate. We adjust the driving so that the saturated value of σ_{3D} is close to the observed size–linewidth relation

$$\sigma_{3D} \approx \sqrt{3}\,(0.72\,km\,s^{-1})\left(\frac{R}{1\rm pc}\right)^{0.5} \approx 3.94\,km\,s^{-1}, \quad (2)$$

where we have let the cloud's radius $R = \ell_0/2 = 10$ pc. The driving power necessary to reach this will vary depending on field strength and equation of state. The values we have adopted for the size–linewidth relation are from Solomon et al. (1987).

The parameters we use are shown in Table 1. Many of these are chosen to reflect values from MML15. We define the plasma β as the ratio of the volume-averaged thermal pressure to the volume averaged magnetic pressure. The Mach number is the mass-weighted rms velocity divided by the mass-weighted sound speed, and the Alfvén Mach number is the mass-weighted rms velocity divided by the volume averaged Alfvén speed. These definitions are chosen so that the Mach number and Alfvén Mach number are simply related to the ratio of kinetic energy to thermal energy and kinetic energy to magnetic energy, respectively. Like MML15, we adopt a constant composition and assume all of our ions are C^+.

We neglect gravity. The total mass in our volume is about 8300 $M_\odot$, giving an overall virial parameter $\alpha_{\rm vir} = 5\sigma_{1D}^2 R/GM \approx 7.2$, rendering self-gravity negligible. We may also compare the effects of

[1] https://github.com/PrincetonUniversity/athena-public-version.

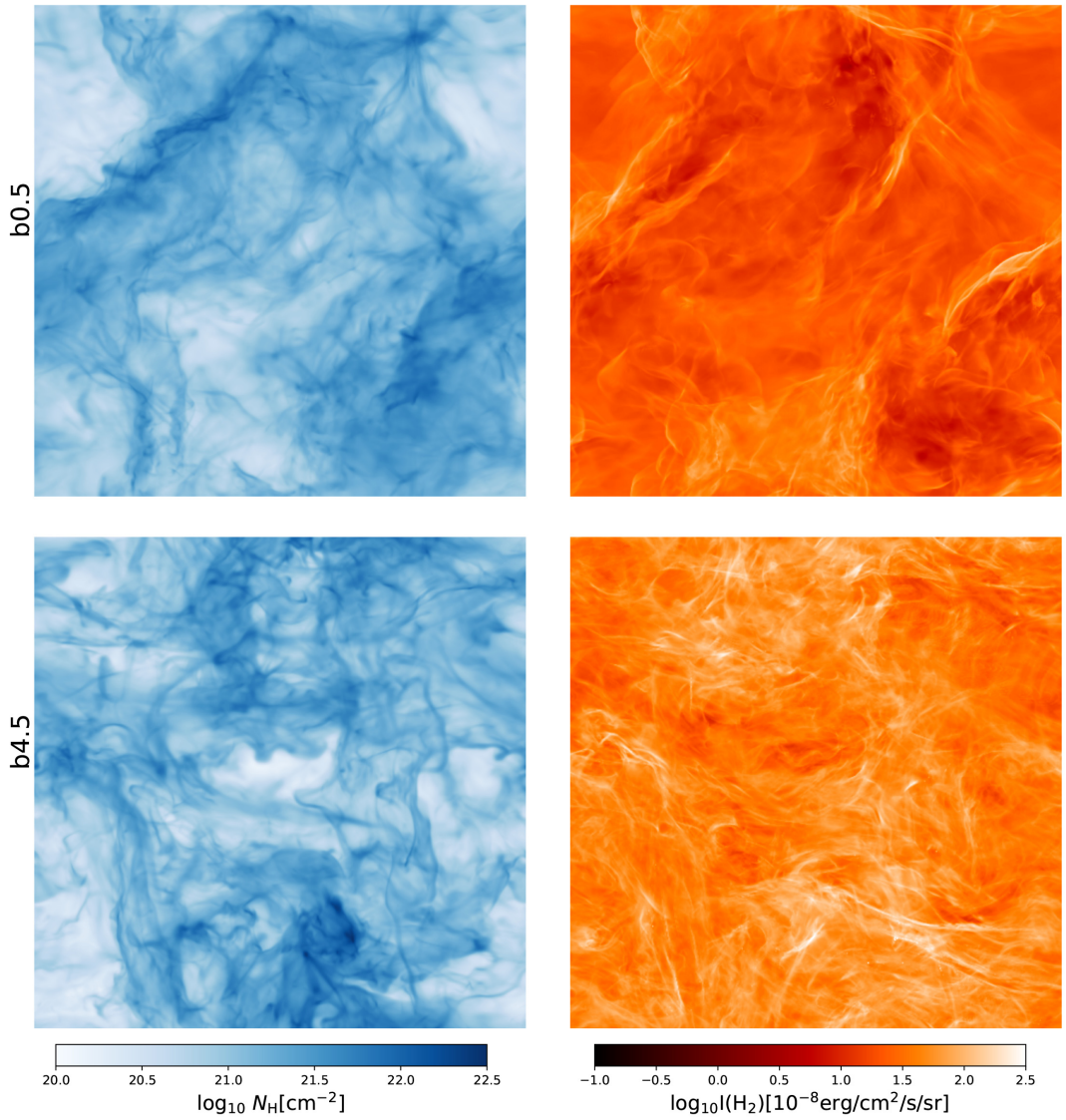

Figure 1. *Left:* Column density of H nuclei in a snapshot of each of our 512^3 ideal MHD simulation including heating and cooling processes. *Right:* Total H_2 rotational line emission intensity. It is apparent that much of the emission comes from shocks by the sheet-like distribution of the emission (see Section 4.2). For each simulation, the box is 20 pc on a side with a mean density of $n_H = 30$ cm^{-3}. The initial (and therefore mean) vector magnetic field $B_0 = 0.5$ μG (top) and 4.5 μG (bottom), oriented in the horizontal direction.

Table 1. Model parameters.

$x(H) \equiv n(H)/n_H$	0.68
$x(H_2) \equiv n(H_2)/n_H$	0.16
$x(He) \equiv n(He)/n_H$	0.1
$x(e^-) \equiv n_e/n_H$	1.6×10^{-4}
$x(C) \equiv n(C^+)/n_H$	1.6×10^{-4}
$x(O) \equiv n(O)/n_H$	3.2×10^{-4}
μ	$1.49 m_{proton}$
$\langle n_H \rangle$	30 cm^{-3}
$\langle \rho \rangle = \mu \langle n \rangle$	7.0×10^{-23} g cm^3
$\langle N_H \rangle = \langle n_H \rangle \ell_0$	1.85×10^{21} cm^{-2}

gravity to magnetic fields through the mass-to-flux ratio relative to critical

$$\mu_\Phi = \frac{2\pi M \sqrt{G}}{B_{rms} \ell_0^2}. \quad (3)$$

For our simulations μ_Φ ranges from about 0.7 to 1.9, so these simulations range from somewhat magnetically sub-critical to somewhat super-critical.

We explicitly follow internal energy in our simulations and changes therein due to heating (from cosmic rays and photoelectric emission from dust grains) and cooling (due to C^+, O, and H_2 line emission). The cooling is not scale-free, introducing a particular length, time, and temperature. When using this cooling function as an explicit source term in a simulation, we are thus given less freedom than when post-processing isothermal simulations.

2.2 Ambipolar diffusion

The effects of ambipolar diffusion in the CNM have been treated in three separate ways in MHD turbulence simulations. The first is to treat ions and neutrals as separate fluids that interact through a drag force with frictional heating (Draine 1986a; Li et al. 2008).

Table 2. Simulation parameters and selected statistics. Simulations labelled with 'iso' employed an isothermal equation of state and are processed differently, as described in Section 3. B_0 and $B_{\rm rms}$ are the mean and rms magnetic field strength; $B_{||,\,\rm rms}$ and $B_{\perp,\rm rms}/\sqrt{2}$ are the root-mean-square (rms) components of the saturated magnetic field along and across the mean magnetic field, respectively; β_0 and β are the initial and final plasma beta; $\sigma_{\rm 3D}$ is the 3D velocity dispersion; $\mathcal{M}_A$ is the final Alfvén Mach number; $\dot{\epsilon}$ is the input driving power/volume; $N_{\rm CH^+,50}$ is the median CH^+ column density; $I_{\rm H_2,50}$ is the median sum total intensity of the H_2 rotational lines; and $\langle \tilde{P}_x \rangle$ and $\langle P_z \rangle$ are the mean magnetic field alignment parameters for viewing along and across the mean magnetic field direction (see Section 6.5).

Name Units	B_0 μG	$B_{\|\|,\,\rm rms}$ μG	$B_{\perp,\rm rms}/\sqrt{2}$ μG	$B_{\rm rms}$ μG	β_0 None	β None	$\sigma_{\rm 3D}$ km s^{-1}	$\mathcal{M}_A$ None	$\dot{\epsilon}$ 10^{-26} erg cm^{-3} s^{-1}	log $N_{\rm CH^+,50}$ log (cm^{-2})	$I_{\rm H_2,50}$ 10^{-8} erg s^{-1} cm^{-2} sr^{-1}	$\langle \tilde{P}_x \rangle$ None	$\langle \tilde{P}_z \rangle$ None
b0.5	0.5	2.4	2.5	4.3	24	0.51	4.3	2.9	7.4	12.2	20.8	0.22	0.22
b0.5-iso	0.5	2.0	2.4	3.7	24	0.68	4.0	3.1	6.7	12.3	20.4	0.18	0.21
b4.5	4.5	6.1	5.1	9.5	0.38	0.10	3.9	1.2	10.0	13.2	45.9	0.27	0.30
b4.5-iso	4.5	5.8	4.4	8.6	0.38	0.13	4.2	1.4	6.7	13.1	47.8	0.24	0.29

This is the most true-to-life of the three methods, but is numerically challenging on the length-scales we are interested in, and currently beyond computational reach.

The second approach is a modified MHD treatment that neglects the inertia of the ions and treats ambipolar diffusion as an extra diffusive term in the magnetic induction equation (Mac Low et al. 1995). It assumes that ions stream relative to the neutrals at an instantaneous velocity given by

$$\boldsymbol{v}_{\rm d} = \frac{(\nabla \times \boldsymbol{B}) \times \boldsymbol{B}}{4\pi \gamma_{\rm AD} \rho_{\rm n} \rho_{\rm i}}, \tag{4}$$

where $\boldsymbol{B}$ is the magnetic field, $\gamma_{\rm AD} = \langle \sigma\ v \rangle / (m_{\rm i} + m_{\rm n})$ is the ion–neutral coupling constant, $\rho_{\rm n}$ is the density of neutral species, and $\rho_{\rm i}$ is the density of ions. Here, $\langle \sigma\ v \rangle$ is the momentum transfer rate coefficient, and $m_{\rm i}$ and $m_{\rm n}$ are the ion and neutral mass per particle. The magnetic field would be evolved according to

$$\frac{\partial \boldsymbol{B}}{\partial t} = \nabla \times ((\boldsymbol{v}_{\rm n} + \boldsymbol{v}_{\rm d}) \times \boldsymbol{B})\ . \tag{5}$$

This second approach is prohibitively expensive for this problem as well. For the 20-pc scales we are interested in, the ambipolar diffusion length is very small in the highest density regions. As a result, to resolve the effects of ambipolar diffusion in these regions would require extremely high resolution. Further, the time-step required for numerical stability in this method scales as $\Delta t_{\rm AD} \propto (\Delta x)^2$, the spatial resolution squared. The combination of these factors makes this approach infeasible for our problem.

The third approach is to assume that ideal MHD can be used to evolve the density, fluid velocity, and magnetic field. An additional approximation often made is that the ion–neutral drift velocity $v_{\rm d}$ can also be approximated by equation (4) with $\boldsymbol{B}$ taken to be the field computed assuming ideal MHD. This approach relies on estimating the effects of ambipolar diffusion in post-processing, rather than self-consistently in real time. Our approach is most similar to this third approach, with some important modifications.

Naively assuming that equation (4) accurately reflects the ion–neutral drift velocities everywhere in a simulation volume leads to several issues. The volume-averaged heating rate calculated with equation (4) can easily exceed the volume-averaged driving power, which is unphysical. The heating power per mass may be very large in low density regions, where the drift velocities given by equation (4) can become very large (see Fig. A1). A conservative way of dealing with these high drift velocities and heating rates is to exclude from our analysis regions where the drift velocity exceeds some chosen threshold. The exact value of this cut will have an effect on our results. Fig. 2 examines the effect that this cut has on our results.

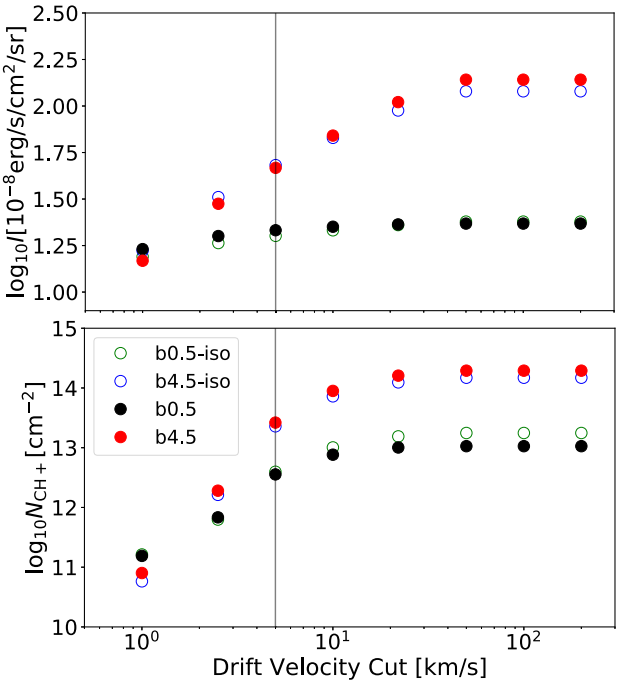

Figure 2. The mean CH^+ column density $N_{\rm CH^+}$ and total H_2 rotational line intensity $I(H_2)$ (defined in Section 6.4) in each simulation as a function of the cutoff in the ion–neutral drift velocity (see Section 6.1). The value we adopt in our analysis, 5 km s^{-1}, limits us to only counting regions where the ambipolar diffusion Reynolds number is greater than order unity ($v_{\rm d} \lesssim \sigma_{\rm 3D}$), as well as ensures that the ambipolar diffusion heating is at most of order the driving energy rate. We show this 5 km s^{-1} cut as a greyed out vertical line.

3 HEATING PROCESSES

As we have simulations with both an isothermal equation of state and a non-isothermal equation of state, we must incorporate heating in two separate ways.

The first (used for the isothermal equation of state) is to determine the temperature in each cell after the simulation is completed assuming a balance between all cooling and heating processes. Formally, a temperature T is computed in each cell where

$$\Lambda(\rho, T) = \Gamma(\rho, \boldsymbol{v}), \tag{6}$$

where $\Lambda(\rho, T)$ (described in Section 4) is the total cooling in that cell and $\Gamma(\rho, \boldsymbol{v})$ is the total heating including cosmic ray and photoelectric heating and an estimate for the viscous heating (see Sections 3.1 and 3.2). Ambipolar diffusion heating is treated differently, and described in Section 3.3.

The second is to use the explicit integration scheme implemented in the MHD code ATHENA++ to include the extra heating and cooling terms (described in Sections 3.1 and 4) dynamically throughout the time domain of the simulation. This method implicitly handles both viscous and shock heating, and has the advantage of allowing for the possibility of adiabatic heating and cooling. However, this can also make the method prohibitively expensive. Occasionally, rarefactions in already cold (dense) gas will adiabatically cool gas well below the equilibrium temperature (which may be as cold as ∼10 K in the case of gas with $n_{\rm H} \sim 10^4 {\rm cm}^{-3}$). For heating that is proportional to density (as in cosmic ray and photoelectric heating, described below in Section 3.1, 3.2), such dense gas may have a large heating rate, but a small internal energy, leading to a restrictive thermal time-step. In this case, we impose a limit on how cold the gas can get, and suppose that it cannot cool below 2.7 K. While this means we effectively inject energy into these few extremely cold regions, the amount is small compared to the other heating terms, and so should have a negligible impact on the global dynamics and chemistry of the simulation.

3.1 Cosmic ray and photoelectric heating

Cosmic ray ionizations and the photoelectric effect on dust grains both serve to heat the cold neutral medium.

The heating due to cosmic ray ionizations is a combination of the cosmic ray ionization rate per hydrogen nucleus $\zeta_{\rm H}$, the heat per ionization ΔQ, and the density $n_{\rm H}$. We take $\zeta_{\rm H} = 1.8 \times 10^{-16}$ s^{-1} from Indriolo & McCall (2012) and $\Delta Q = 10$ eV from Glassgold, Galli & Padovani (2012).

Our chosen ΔQ and $\zeta_{\rm H}$ are identical to those chosen in MML15 so that our results are as directly comparable as possible. The cosmic ray heating is thus

$$\Gamma_{\rm CR} = \zeta_{\rm H} \Delta Q n_{\rm H} = 1.9 \times 10^{-25} \left(\frac{n_{\rm H}}{\langle n_{\rm H} \rangle} \right) {\rm erg\,cm^{-3}\,s^{-1}}. \quad (7)$$

The dust photoelectric heating rate can be written (Wolfire et al. 2003)

$$\Gamma_{\rm PE} = 1.3 \times 10^{-24} n_{\rm H} \epsilon G_0 \,{\rm erg\,cm^{-3}\,s^{-1}}, \quad (8)$$

with ϵ being the heating efficiency and G_0 the FUV intensity in the units of Habing (1968). For $G_0 = 1.1$ (Mathis, Mezger & Panagia 1983), and typical parameters ($\langle n_{\rm H} \rangle = 30\,{\rm cm^{-3}}$, $T = 100$ K, $x(e) = 1.6 \times 10^{-4}$), $\epsilon = 0.018$, and thus

$$\Gamma_{\rm PE} = 7.6 \times 10^{-25} \left(\frac{n_{\rm H}}{\langle n_{\rm H} \rangle} \right) {\rm erg\,cm^{-3}\,s^{-1}}, \quad (9)$$

four times larger than $\Gamma_{\rm CR}$.

3.2 Viscous heating

While viscous heating is handled implicitly in ATHENA++ when we use a non-isothermal equation of state, for simulations with an isothermal equation of state we determine the temperature using a post-processing scheme similar to that in Pan & Padoan (2009) and MML15. To estimate the viscous heating in each cell of the simulation, we first compute the rate of shear tensor $\boldsymbol{\sigma}$

$$\boldsymbol{\sigma} = \frac{1}{2}(\nabla \boldsymbol{v} + \nabla \boldsymbol{v}^T) - \frac{1}{3}(\nabla \cdot \boldsymbol{v})\boldsymbol{\delta}, \quad (10)$$

where T denotes the transpose, and $\boldsymbol{\delta}$ is the euclidean metric tensor. The gradients here are determined using a cell-centred finite difference method, and so should be second-order accurate in the spatial resolution. Given $\boldsymbol{\sigma}$, the viscous heating in a cell is

$$\Gamma_\nu = 2\nu\rho\boldsymbol{\sigma} : \boldsymbol{\sigma}. \quad (11)$$

The kinematic viscosity ν here is not of physical origin; it is a numerical viscosity. Similarly to MML15, we estimate its value by allowing ν to be a normalization such that the total viscous heating in the simulation is equal to the input driving power; in other words, we assume that all the input driving power goes into viscous heating.

3.3 Ambipolar diffusion heating

We do not include ambipolar diffusion in the dynamics of our simulation. However, in low density regions, ambipolar diffusion can become an important heating mechanism. In order to best estimate what the thermal effects of ambipolar diffusion *would be* in our simulations, we begin with the temperature T either from the code directly (as is the case with simulations b0.5 and b4.5), or post-processed following a procedure similar to that given in MML15 (done for the isothermal simulations b0.5-iso and b4.5-iso). Given these temperatures T, we compute a new temperature $T_{+\rm AD}$ by solving the following equation in each cell of the simulation:

$$\Lambda(\rho, T_{+\rm AD}) = \Gamma_{\rm AD}(\rho, \boldsymbol{B}) + \Lambda(\rho, T), \quad (12)$$

where $\Gamma_{\rm AD}$ is the heating rate per volume due to ion–neutral friction. This may be expressed as

$$\Gamma_{\rm AD} = \gamma_{\rm AD} \rho_{\rm n} \rho_{\rm i} v_{\rm d}^2, \quad (13)$$

where $\gamma_{\rm AD} = \langle \sigma\, v \rangle / (m_{\rm n} + m_{\rm i})$ is the ion–neutral coupling coefficient (taken to be between C^+ ions and H_2, identical to that in equation 4), and $v_{\rm d}$ is the ion–neutral drift velocity (see equation 4). This assumes instantaneous balance between heating and cooling, which will only be approximately true. It is important to note, however, that this does not throw out our hard-earned dynamical heating, as the new temperature $T_{+\rm AD}$ is bounded by the old temperature T from below, or

$$T_{+\rm AD} \geq T. \quad (14)$$

4 COOLING PROCESSES

4.1 Fine structure lines

In the cold neutral medium, the main avenues for cooling we expect are due to the species C^+, O, and H_2. For C^+ and O, we use

$$\Lambda_{\rm C^+}/n_{\rm H}^2 = 3.6 \times 10^{-27} {\rm e}^{-92\,{\rm K}/T} {\rm erg\ cm^3\ s^{-1}} \quad (15)$$

$$\Lambda_{\rm O}/n_{\rm H}^2 = 2.35 \times 10^{-27} \left(\frac{T}{100\,{\rm K}} \right)^{0.4} {\rm e}^{-228\,{\rm K}/T} {\rm erg\ cm^3\ s^{-1}}. \quad (16)$$

These values have been scaled from their original values in Wolfire et al. (2003) to reflect our C and O abundances.

4.2 H_2 line emission

The rotation-vibration lines of H_2 can be important cooling channels. We employ a new H_2 cooling function that is easy to evaluate, but which provides a good approximation to detailed calculations of H_2 excitation over a wide range of densities, temperatures, and molecular fractions. Our new cooling function $\Lambda_{\rm H_2}$ is based on up-to-date collisional rate coefficients, as described in Appendix B. Fig. 3 shows the cooling rate for $n_{\rm H} = 30\,{\rm cm^{-3}}$ and molecular fraction $2n({\rm H_2})/n_{\rm H} = 0.3$ that MML15 took to be a representative example

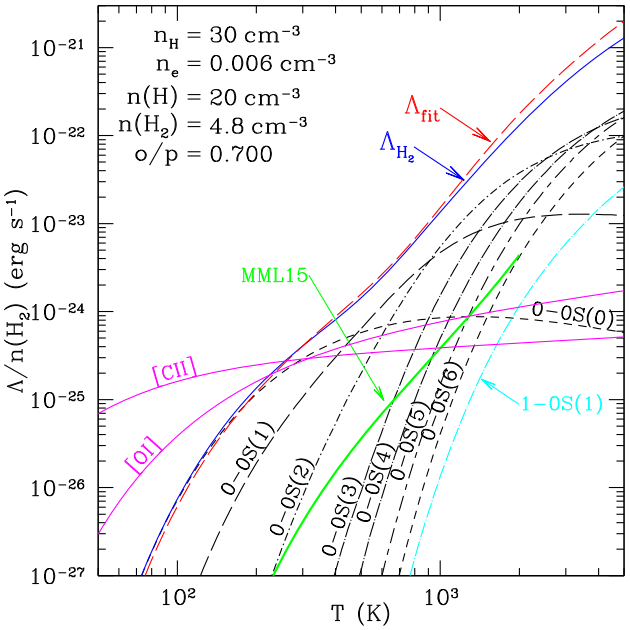

Figure 3. Solid line: $\Lambda_{H_2}/n(H_2)$ power radiated per H_2 for statistical equilibrium (equation B14), Red curve: $\Lambda_{fit}/n(H_2)$ (equation 17). Contributions to the cooling of selected lines are shown. The magenta curves show the radiated power (per H_2) from [C II]158 μm and [O I]63 μm. Also shown (green curve) is the H_2 cooling per H_2 given by MML15. Our cooling function Λ_{H_2} exceeds the MML15 H_2 cooling function by a factor ∼40 for $T \gtrsim 500$ K.

for gas in a turbulent molecular cloud. We fix the ortho/para ratio at the value 0.7 adopted by MML15. The H_2 cooling for this case is shown in Fig. 3.

The total H_2 cooling is shown (blue solid curve) for $100\,\mathrm{K} \leq T \leq 5000\,\mathrm{K}$. Also shown are the powers in selected emission lines. For $T \leq 10^3$ K, the H_2 cooling is dominated by four rotational lines: $0-0S(0)28.22$, $0-0S(1)17.03$, $0-0S(2)12.28$, and $0-0S(3)9.66$ μm. At temperatures $T \gtrsim 1000$ K, rotational lines from $J > 5$ become important, and for $T > 2000$ K the vibrational transitions (e.g. $1-0S(1)2.122$ μm) begin to make a significant contribution to the total cooling.

In Fig. 3, we also show the cooling power (per H_2 molecule) in the [C II]158 μm and [O I]63 μm fine structure lines. We see that for the conditions considered in Fig. 3, the fine structure lines dominate the cooling for $T \lesssim 300$ K, but for $T \gtrsim 300$ K the cooling is dominated by H_2.

Fig. 3 also shows the H_2 cooling function from MML15, for $T \lesssim 2000$ K. The MML15 cooling function is smaller than the present Λ_{H_2} by a factor ∼40.

The resulting cooling power per H_2, $\Lambda/n(H_2)$, is shown in Fig. 4 for selected densities $1 \leq n_H \leq 10^5$ cm^{-3}, for gas that is predominantly atomic (Fig. 4a) and predominantly H_2 (Fig. 4b). The atomic and molecular cases differ because the rate coefficients for collisional excitation of H_2 by H and by H_2 can in some cases differ by large factors. For example, at $T = 5000$ K, the cooling power per H_2 is ∼5 times larger in atomic than in molecular gas with the same n_H.

At densities $n_H \lesssim 10^2$ cm^{-3}, $\Lambda_{H_2}/n(H_2)$ is approximately linear in n_H, with almost all collisional excitations followed by radiative decay. At high densities $n_H \gtrsim 10^5$ cm^{-3}, the level populations approach LTE, and $\Lambda_{H_2}/n(H_2)$ becomes independent of density.

For computational purposes, it is useful to have an analytical function $\Lambda_{fit}(n, T)$ that provides an acceptable approximation to the 'exact' H_2 cooling function $\Lambda_{H_2}(T)$ for $T \lesssim 5000$ K

$$\Lambda_{fit} = n(H_2)\sum_{i=1}^{4} f_i(n,T)$$

$$f_1(n,T) = 1.1{\times}10^{-25} T_3^{0.5} e^{-0.51/T_3}\left[\frac{0.7x_1}{1+x_1/n_1} + \frac{0.3x_1}{1+x_1/(10n_1)}\right] \mathrm{erg\,s^{-1}}$$

$$f_2(n,T) = 2.0{\times}10^{-25} T_3 e^{-1/T_3}\left[\frac{0.35x_2}{1+x_2/n_2} + \frac{0.65x_2}{1+x_2/(10n_2)}\right] \mathrm{erg\,s^{-1}}$$

$$f_3(n,T) = 2.4{\times}10^{-24} T_3^{1.5} e^{-2/T_3}\left[\frac{x_3}{1+x_3/n_3}\right] \mathrm{erg\,s^{-1}}$$

$$f_4(n,T) = 1.7{\times}10^{-23} T_3^{1.5} e^{-4/T_3}\left[\frac{0.45x_4}{1+x_4/n_4} + \frac{0.55x_4}{1+x_4/(10n_4)}\right] \mathrm{erg\,s^{-1}} \quad (17)$$

$$x_1 \equiv n(H) + 5.0n(H_2) \qquad n_1 = 50\,\mathrm{cm^{-3}} \quad (18)$$

$$x_2 \equiv n(H) + 4.5n(H_2) \qquad n_2 = 450\,\mathrm{cm^{-3}} \quad (19)$$

$$x_3 \equiv n(H) + 0.75n(H_2) \qquad n_3 = 25\,\mathrm{cm^{-3}} \quad (20)$$

$$x_4 \equiv n(H) + 0.05n(H_2) \qquad n_4 = 900\,\mathrm{cm^{-3}} \quad (21)$$

The coefficients multiplying $n(H_2)$ in equations (18)–(21) reflect the collisional rate coefficients for excitation by H_2 relative to excitation by H and He. We see that equation (17) provides a fairly good fit to Λ over a wide range of temperatures and densities, for both atomic gas (Fig. 4a) and molecular gas (Fig. 4b).

Coppola et al. (2019, hereafter CLM19) provide a fitting function for H_2 cooling over the 10^2–4000 K temperature range. Fig. 4 compares the CLM19 fitting function to our calculated H_2 cooling rates in predominantly atomic gas: the CLM19 fitting function tends to underestimate our computed cooling rates by factors of ∼2 for $T \lesssim 500$ K.

Both CLM19 and this study use H–H_2 collision cross-sections from Lique (2015). The difference in the $T \lesssim 500$ K cooling appears to be due to differences in adopted rates for collisional excitation by He: Coppola et al. (2019) used quasi-classical trajectory cross-sections from Celiberto et al. (2017) whereas we use quantum-mechanical results from Le Bourlot, Pineau des Forêts & Flower (1999), which are believed to be more accurate at low energies.

For molecular gas, the CLM19 fitting function underestimates the cooling rate by a factor of ∼3 for temperatures $\lesssim 500$ K, and overestimates it by a similar factor for $\gtrsim 500$ K. Both this study and CLM19 assume ortho-para equilibration, resulting in a low ortho-para ratio at the lower temperatures.

5 CH^+ CHEMISTRY

When ions are streaming through the neutrals, the rate for the endothermic reaction (1) is affected by the non-thermal distribution of ion–neutral impact speeds. Following Flower et al. (1985), we employ a rate coefficient that is a function of an effective temperature

$$T_{eff} = T_{+AD} + \frac{\mu}{3k}v_d^2 = T_{+AD} + 10^3\mathrm{K}\left(\frac{v_d}{3.8\,\mathrm{km\,s^{-1}}}\right)^2, \quad (22)$$

where μ is the reduced mass of C^+ and H_2 and k is the Boltzmann constant. This applies when $T_{eff} \geq 1547$ K (Pineau des Forets et al. 1986). When $T_{eff} < 1547$ K, we instead have that the reaction rate is a function of

$$T' \equiv T_{+AD}\frac{4640\,\mathrm{K}}{4640\,\mathrm{K} - \mu v_d^2/k} \approx \frac{T_{+AD}}{1-(v_d/4.7\,\mathrm{km\,s^{-1}})^2} \quad (23)$$

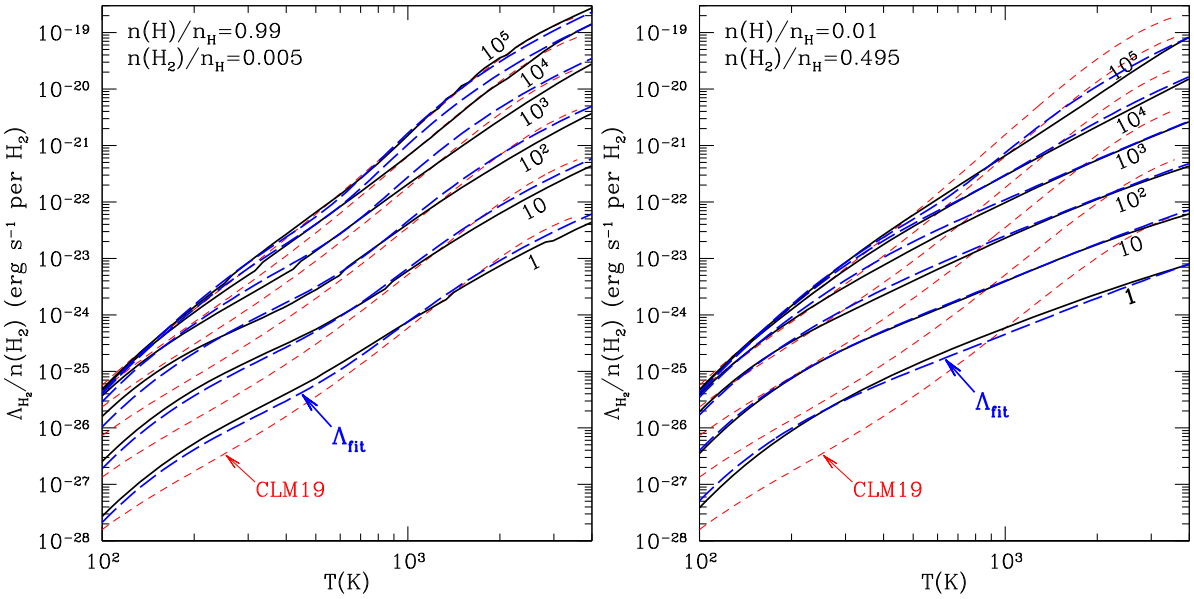

Figure 4. H_2 cooling power per H_2 for densities $n_H = 1$, 10, 10^2, 10^3, 10^4, and 10^5 cm^{-3}. (a) Gas which is 99 per cent atomic and 1 per cent H_2 (b) Gas which is 99 per cent H_2 and 1 per cent atomic. Solid curves: present calculations. Blue dashed curves: fitting function $\Lambda_{\rm fit}$ (equation 17). Red dashed curves: CLM19 fitting function. $\Lambda_{\rm fit}$ (equation 17) is much closer to our exact calculation than the CLM19 fit. Differences are most pronounced for gas that is mainly H_2.

As with MML15, we assume instantaneous balance between formation and destruction of CH^+. The rate coefficients for each of the various creation and destruction mechanisms are

$$\begin{aligned}
C^+ + H_2 \rightarrow CH^+ + H;\ \ k_{CH^+} &= 2.6\times10^{-10}\exp[-\xi]\,{\rm cm^3\,s^{-1}},\\
\xi &\equiv \max\left\{\frac{4640\,{\rm K}}{T_{\rm eff}}, \frac{4640\,{\rm K}}{T'}\right\},\\
C^+ + H \rightarrow CH^+;\ \ k_{\rm ra} &= 4.46\times10^{-17}T_2^{-1/2}\\
&\quad\times\exp\left[-0.229T_2^{-2/3}\right]\ {\rm cm^3\,s^{-1}},\\
CH^+ + H \rightarrow C^+ + H_2;\ \ k_{\rm H1} &= 1.5\times10^{-10}\,{\rm cm^3\,s^{-1}},\\
CH^+ + H_2 \rightarrow CH_2^+ + H;\ \ k_{\rm H_2} &= 1.2\times10^{-9}\,{\rm cm^3\,s^{-1}},\\
CH^+ + e \rightarrow C + H;\ \ k_e &= 5.2\times10^{-8}T_2^{-0.17}\,{\rm cm^3\,s^{-1}} \qquad (24)
\end{aligned}$$

k_{CH^+} is an approximate form given by Pineau des Forets et al. (1986), but increased by a factor 2.6 to better match the exact rate shown in Fig. 5. In Fig. 5, we compare the Pineau des Forets et al. (1986) approximation against the 'exact' rate in Fig. 5 is calculated following Draine & Katz (1986a) for various v_d using the cross-section for the $v = 0, J = 0$ state of H_2 (Gerlich, Disch & Scherbarth 1987; Zanchet et al. 2013). $k_{\rm H1}$, and $k_{\rm H_2}$ are those from the Meudon PDR code.[2] $k_{\rm ra}$ is from Barinovs & van Hemert (2006), while k_e is from Chakrabarti et al. (2018). Balancing formation with destruction gives

$$n_{CH^+} = x(C^+)\frac{x(H_2)k_{CH^+} + [1-2x(H_2)]k_{\rm ra}}{[1-2x(H_2)]k_{\rm H1} + k_{H_2}x(H_2) + k_e x(e)}n_H. \qquad (25)$$

It is clear from this expression that the CH^+ abundance is most sensitive to the abundances of C^+ and H_2. Solving for the abundance as a function of time when perturbed from equilibrium, one finds that the chemical relaxation time is of the order of 250 yr, much shorter than all other time-scales in our simulation, so the assumption of equilibrium chemistry is a good one.

[2]https://ism.obspm.fr/?page_id = 33.

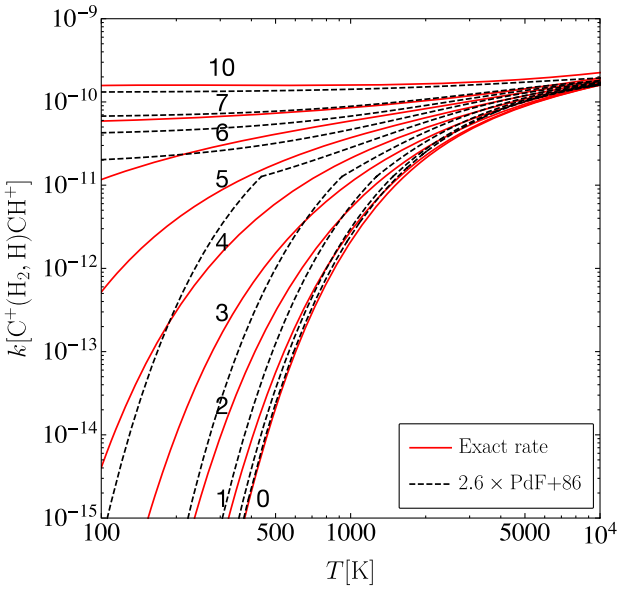

Figure 5. The exact rate coefficient (red, solid) for the reaction (1) (see text) and the approximation (black, dashed) from Pineau des Forets et al. (1986), but multiplied by 2.6 to better match the exact rate. The exact curves are labelled by the ion–neutral drift velocity v_d (km s^{-1}). The approximate curves correspond sequentially to these same drift velocities. We see that the approximation is more accurate at higher values of the rate coefficient, with the largest discrepancies being when the drift velocities are 5 and 6 km s^{-1}.

6 RESULTS

6.1 Temperature and ion–neutral drift

The chemistry we are primarily interested in takes place in gas with temperatures $\gtrsim$1000K. Fig. 6 shows that in our simulations, the mass-fraction of the gas with either $T_{+\rm AD} \gtrsim 1000$ K or $T_{\rm eff} \gtrsim 1000$ K

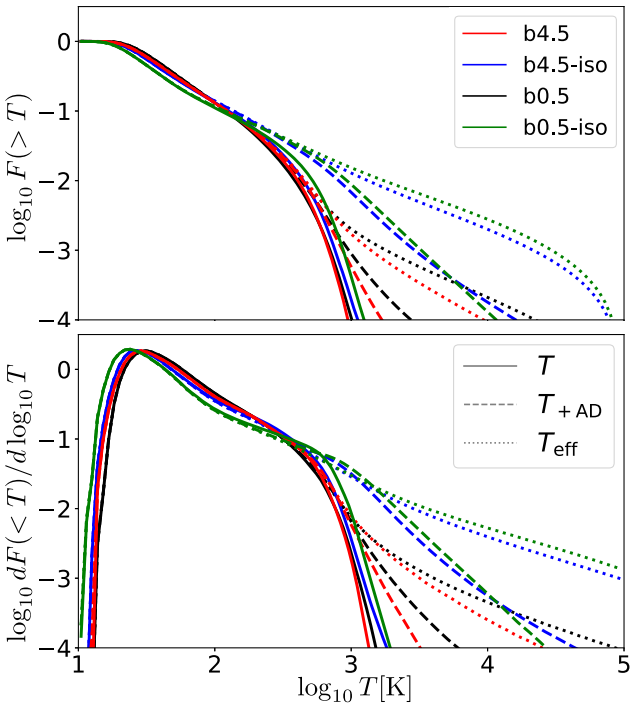

Figure 6. Mass weighted cumulative distribution functions (top) and probability density functions (bottom) of temperature T (solid), temperature adjusted with ambipolar diffusion heating $T_{+\mathrm{AD}}$ (dashed, see equation 12), and effective temperature (dotted, see equation 22) for simulations with two different mean magnetic field strengths and either an isothermal equation of state post-processed as described in Section 3. It is clear that the difference between the two procedures is not dramatic. Further, as might be expected, for higher field strengths, the PDFs for $T_{+\mathrm{AD}}$ and T_{eff} show a much larger mass of gas at or above 1000 K, and thus able to produce CH^+ and H_2 rotational line emission.

is ~ 1 *per cent*, just as Falgarone & Puget (1995) and Pan & Padoan (2009) suggested was necessary to produce the observed column densities of CH^+. If the temperature becomes *too* high, ($\gtrsim$ 5000 K) molecular hydrogen will be dissociated. We also suppose that CH^+ production will cease if the ion–neutral streaming velocity v_{d} exceeds $\sim$22 km s^{-1}, where the centre-of-mass energy is sufficient to dissociate H_2 via $C^+ + H_2 \rightarrow C^+ + 2H$.

With ideal MHD, we find the drift velocities given by equation (4) can sometimes become very large in low density regions, sometimes reaching values as large as 100 km s^{-1} in very low density regions. In nature, were drift velocities this high produced, they would (1) self-limit by decreasing the magnetic field strength directly through diffusion, and (2) create high ambipolar diffusion heating rates that would drive up the temperature and thus ionization of the gas, leading to stronger ion–neutral coupling and a drop in the drift speed. We thus suspect that in the cold neutral medium, drift velocities do not routinely reach these high values $v_{\mathrm{d}} \gtrsim 5$ km s^{-1}. For these reasons, we choose to simply ignore CH^+ production in regions in our simulation where the drift velocity exceeds 5 km s^{-1}. We explore the effect of varying this cut-off velocity in Fig. 2.

6.2 CH^+ abundance

With the CH^+ formation rate depending on the effective temperature T_{eff}, we expect the CH^+ abundance to be biased towards both high T and high ion–neutral drift velocity regions. These regions happen to mostly coincide. In Fig. 7, we show joint histograms of T versus drift velocity, T versus density, and drift velocity versus density for each of our four simulations. The white contours in Fig. 7 represent where 99 per cent, 90 per cent, and 50 per cent of the CH^+ exists on each plot. These contours demonstrate that in all of our simulations, CH^+ is produced in low density ($n_{\mathrm{H}} \sim 3$ cm^{-3}), high drift velocity ($v_{\mathrm{d}} \gtrsim 1$ km s^{-1}), hot regions ($T \gtrsim 500$ K).

However, these two modes for creating CH^+ are not equal in efficacy. For both the high field strength simulations (b4.5 and b4.5-iso) and the low field strength simulations (b0.5 and b0.5-iso), it seems that high drift velocity regions are responsible for the vast majority of CH^+ production. Fig. 2 shows that when we exclude regions with $v_{\mathrm{d}} \geq v_{\mathrm{cut}}$, as we decrease v_{cut}, the CH^+ abundance in the simulations is attenuated beginning at about $v_{\mathrm{cut}} \approx 20$ km s^{-1} in all simulations. As we reduce v_{cut} down to 1 km s^{-1} nearly all of the CH^+ vanishes, with our abundances falling to between 10^{10} and 10^{11} cm^{-2}.

As another way to estimate the effect of ion–neutral drift on CH^+, we may use the ordinary temperature T instead of $T_{+\mathrm{AD}}$ or T_{eff} in computing the CH^+ abundance using equation (25). Doing so, we find median CH^+ column densities that are lower than those listed in Table 2 by a factor of between 16 and 50 (depending on the simulation), far below those observed in Weselak et al. (2008). This suggests that ion–neutral drift is critical for CH^+ formation.

In Figs 8 and 9, we compare the results of our model to Weselak et al. (2008)'s data. Fig. 8 shows reasonable agreement between the Weselak et al. (2008) data and our simulations b4.5 and b4.5-iso, though there may be a larger tail to low CH^+ column density in the observations than in our simulation data. In Fig. 9, we do not find the same correlation between column density of H nuclei and CH^+ in our simulations that seems to be present in the Weselak et al. (2008) sample.

Our simulations assume a constant H_2 fraction, $n(H_2) = 0.16 n_{\mathrm{H}}$ – we do not follow formation and destruction of H_2, which would require treating the radiative transfer of the far-UV photons responsible for photodissociation of H_2. Thus the low N_{H} sightlines in our simulations support CH^+ formation via reaction (1). In the real ISM, however, sightlines with $N(H_2) \lesssim 10^{18}$ cm^{-2} tend to have low H_2 fractions, because photodissociation is insufficiently suppressed by self-shielding (Draine & Bertoldi 1996) – this accounts for the absence of CH^+ detections for $N_{\mathrm{H}} < 2.5 \times 10^{20}$ cm^{-2} in Weselak et al. (2008).

Our simulations were limited to a single $20 \times 20 \times 20$ pc^3 molecular region, whereas observations may sample molecular regions that are both smaller and larger. However, our simulated $20 \times 20 \times 20$ pc^3 simulations are quite clumpy, so that sightlines sample column densities N_{H} ranging from $10^{20.3}$ to 10^{22} cm^{-2} (see Figs 1 and 9), similar to the range of N_{H} values in the Weselak et al. (2008) sample.

In this study, we define $I(H_2)$ as the intensity of emission from the first three H_2 rotational lines 0-0 $S(0)$, $S(1)$, and $S(2)$. How it is computed from the simulations and observational data is specified in Section 6.4. Comparing N_{CH^+} to $I(H_2)$, Fig. 10 shows a strong correlation between these quantities, in particular where column densities of CH^+ are high or where $I(H_2)$ is high. This is in line with the observed correlation of rotationally excited H_2 with N_{CH^+} (Spitzer, Cochran & Hirshfeld 1974; Frisch & Jura 1980; Lambert & Danks 1986).

Fig. 11 shows the joint probability density function of magnetic field strength versus number density of hydrogen nuclei, with contours containing 50 per cent, 90 per cent, and 99.9 per cent of the

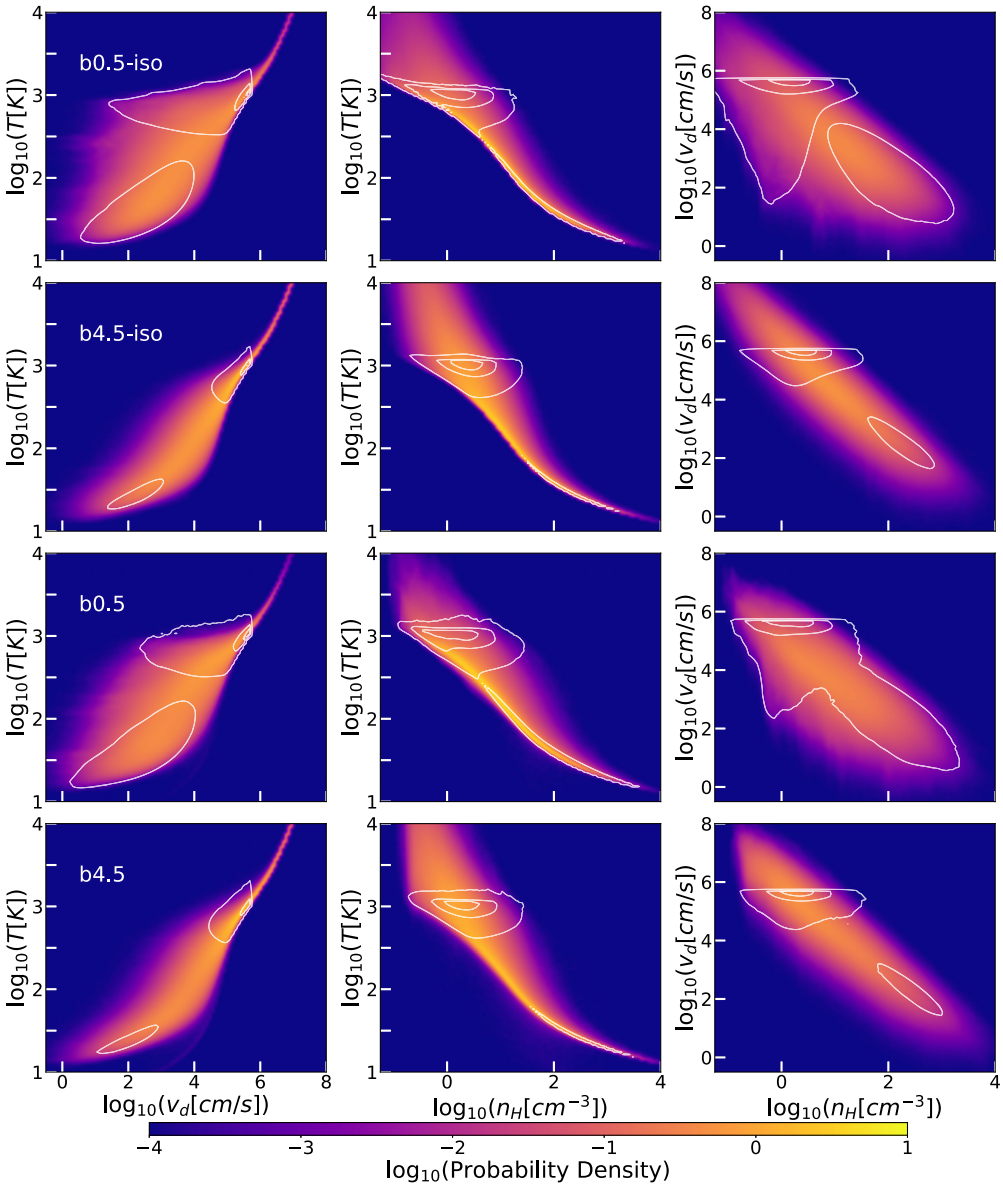

Figure 7. Left: The joint probability density function of gas temperature T and ion–neutral drift velocity v_d (see Sections 2.2 and 3). The white contours contain 50 per cent, 90 per cent, and 99.9 per cent of the CH^+. This is true for the contours across the other columns as well. Middle**:** Joint PDF for temperature and density n_H. The scatter above the density dependent equilibrium is due to additional heating due to shear viscosity, shock heating (in the case of b0.5 and b4.5), and ambipolar diffusion. Right: Joint PDF for v_d and n_H. The temperatures plotted here are those referred to as $T_{+\mathrm{AD}}$ in the text; that is, they include ambipolar diffusion heating in their determination.

CH^+ in our simulation. As CH^+ appears to cluster around densities $n_\mathrm{H} \sim 1\,\mathrm{cm}^{-3}$ in our simulations, we may consider the CH^+ column density to be a probe of the heating processes in the lowest density molecular regions.

6.3 Synthetic CH^+ velocity distributions

We construct synthetic line-of-sight (1D) particle velocity distributions for H_2 and CH^+ for qualitative comparison with observations (e.g. Pan et al. 2004). In each cell of a simulation, we have the neutral fluid velocity $\boldsymbol{v}$ and the ion–neutral drift velocity $\boldsymbol{v}_\mathrm{d}$ (calculated as in equation 4). The fluid velocity of the ions in that cell is

$$\boldsymbol{v}_\mathrm{i} = \boldsymbol{v} + \boldsymbol{v}_\mathrm{d}. \tag{26}$$

We assume Maxwellian velocity distributions, centred on $\boldsymbol{v}$ for neutrals, and $\boldsymbol{v}_\mathrm{i}$ for ions. In addition, below the grid scale of the simulation, there will be some microturbulent contribution to the velocity dispersions of both the ionic and neutral species. If the power spectrum for each simulation were purely Kolmogorov, this microturbulent contribution would be $\sigma_0 \approx 0.5\,\mathrm{km\,s}^{-1}$, and this is the value we assume. The total width of the velocity distribution for a species X in a cell j is therefore

$$\sigma^2_{X,j} = \frac{kT_{X,j}}{m_X} + \sigma_0^2, \tag{27}$$

where k is the Boltzmann constant, $T_{X,j}$ is the kinetic temperature of species X in cell j, and m_X is the mass of species X.

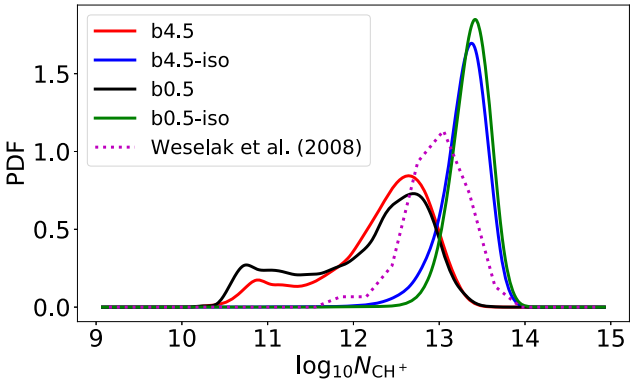

Figure 8. Probability density functions for the (log) column density of CH^+ in each of our four simulations, computed as described in Section 6.2. The solid magenta line corresponds to data from Weselak et al. (2008). The high magnetic field strength simulations, b4.5 and b4.5-iso somewhat exceed the Weselak et al. (2008) data. The low field strengths (b0.5 and b0.5-iso) fall short of explaining the observations.

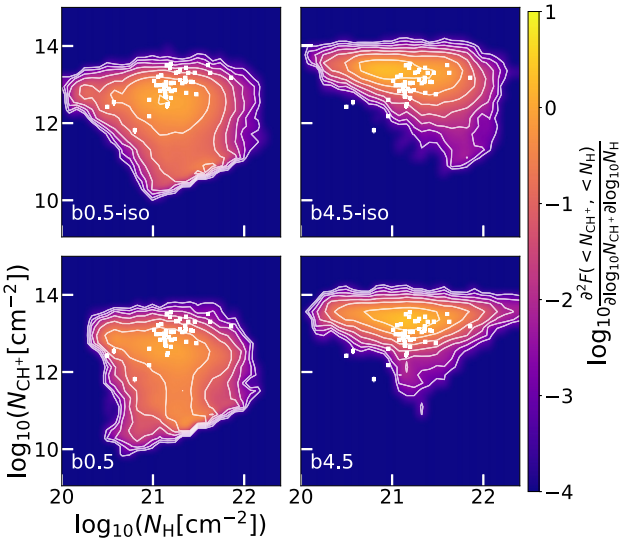

Figure 9. Joint histograms of the column density of CH^+ and N_H for 512^2 sightlines in each simulation (note: this plot is insensitive to viewing angle). The white data points are from Weselak et al. (2008). Contours reflect the levels of the PDF every 1/2 dex. Our b4.5 model does seem to reproduce the abundances seen in Weselak et al. (2008). However, it should be noted that we have omitted CH^+ in regions where the ion–neutral drift velocity v_d exceeds 5 km s^{-1}.

The velocity profile $dN^{(X)}/du$ of a species X at a velocity u is

$$\frac{dN^{(X)}}{du} = \Delta x \left(\frac{\pi}{2}\right)^{1/2} \sum_{j=1}^{N} \frac{n_j^{(X)}}{\sigma_{X,j}} \exp\left(-(u - v_{X,j})^2/2\sigma_{X,j}^2\right), \quad (28)$$

where $n_{X,j}$ is the number density of species X in cell j, and Δx is the physical size of a cell.

Equation (27) has a species specific temperature, T_X for the possibility of ions being out of thermal equilibrium with the neutral species. Ion–neutral scattering will heat the ions to a temperature

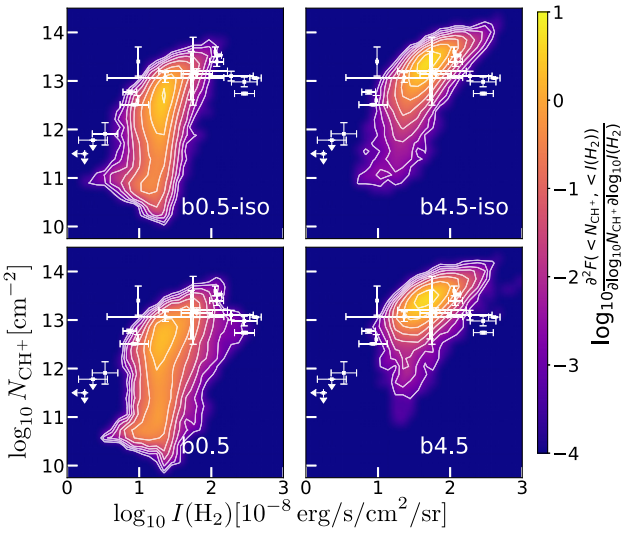

Figure 10. Joint histograms of the column density of CH^+ and the total intensity in H_2 rotational line emission, I($S(0) + S(1) + S(2)$). A strong correlation exists between the two quantities at higher column densities of CH^+. The H_2 data are collated from Spitzer et al. (1974), Snow (1976), Black & Dalgarno (1977), Frisch (1980), Frisch & Jura (1980), Gry et al. (2002), and Lacour et al. (2005). The CH^+ data are from Hobbs (1973), Chaffee (1975), Frisch (1979), Frisch & Jura (1980), Lambert & Danks (1986), Gry et al. (2002), and Weselak et al. (2008).

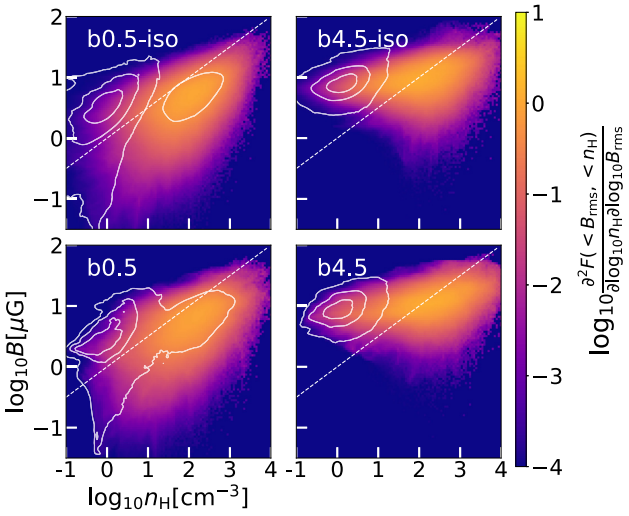

Figure 11. Joint probability densities of the (log) magnetic field at each position in our simulations versus the (log) density of hydrogen nuclei. Contours represent 50 per cent, 90 per cent, and 99.9 per cent of the CH^+ in the volume. The dashed line represents the scaling $B \propto \sqrt{\rho}$. For $B_0 = 0.5$ μG simulations where most of the field strength is generated by the turbulence and $\mathcal{M}_A \approx 3$ (b0.5, b0.5-iso), the scaling $B \propto \sqrt{\rho}$ is approximately followed, albeit with large scatter. However, for $B_0 = 4.5$ μG simulations with $\mathcal{M}_A \approx 1$ (b4.5 and b4.5-iso), there is not much dependence of the magnetic field on density.

where heat transfer to and from the ions (Draine 1986a) vanishes

$$T_i \approx T_{+AD} + \frac{1}{3k} m_n v_d^2, \quad (29)$$

where m_n is the mean mass of the neutrals (see Table 1), and k is the Boltzmann constant.

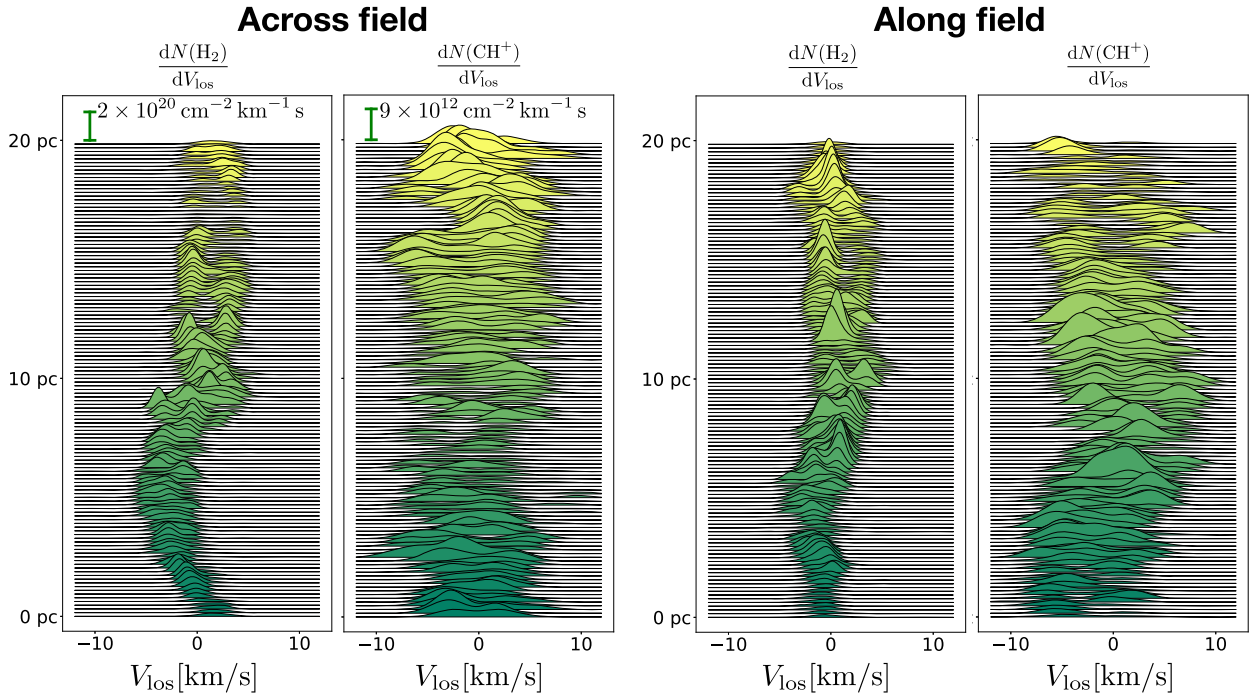

Figure 12. *Left:* Line-of-sight velocity profiles for H_2 molecules and CH^+ molecules computed looking across the mean magnetic field. These are for the simulation b4.5 (see Tab. 2). The vertical offset increases linearly with a coordinate perpendicular to the line of sight and $\mathbf{B}_0$. For scale, two green bars are provided to indicate the height of the profiles. In all panels, colour simply shows progression from one side of the simulation to the other. *Right:* The same, but computed looking along $\mathbf{B}_0$. The scales are the same as the corresponding scale bars on the left. We see considerable diversity among the CH^+ line profiles, and no obvious correlation with the H_2 profiles. The CH^+ profiles are also consistently wider, with a width $\sim$10 km s^{-1}, while the H_2 only has a width of at most a few km s^{-1}.

Constructing these velocity profiles for CH^+ and H_2 in our simulations (Fig. 12), we see that the CH^+ is consistently broader than the H_2 velocity profiles. As well, we often see multiple components of CH^+, sometimes separated by 10 km s^{-1}. For neutral line profiles, while we do see multiple components, as $\sigma_{3D} \approx 4$ km s^{-1}, we do not see component separations of more than a few km s^{-1}.

6.4 H_2 rotational line emission, $0-0\,S(n)$

Fig. 13 shows the intensity of H_2 rotational emission lines $0-0$ $S(n)$ from $n = 0$ through $n = 8$ in each of our simulations, computed using the temperature T_{+AD}. As is the case with all of our analysis in this paper, we exclude regions where the ion–neutral drift velocity exceeds 5 km s^{-1}. The higher field strength simulations (b4.5 and b4.5-iso) exhibit a notably higher level of emission compared to the low field strength simulations (b0.5 and b0.5-iso), especially at higher n. Even with the obvious enhancement of the line intensities from the ambipolar diffusion heating, we still do not reach the line intensities seen by Ingalls et al. (2011) at four positions on the high-latitude translucent cloud Dcld 300.2-16.9. Other excitation mechanisms appear to be necessary to explain the Ingalls et al. (2011) intensities. However, our simulations *do* largely agree with other data. In Fig. 13, we also plot median values of the intensity of $0-0$ $S(0)$, $S(1)$, and $S(2)$ for AGN sightlines from Wakker (2006) and Gillmon et al. (2006) towards AGN. As well, the data in Fig. 10 from Lambert & Danks (1986), Spitzer et al. (1974), and Frisch & Jura (1980) show good agreement with both of our simulations.

As mentioned in Section 6.2, one point of comparison between observations and our simulations we use is the sum of the intensities

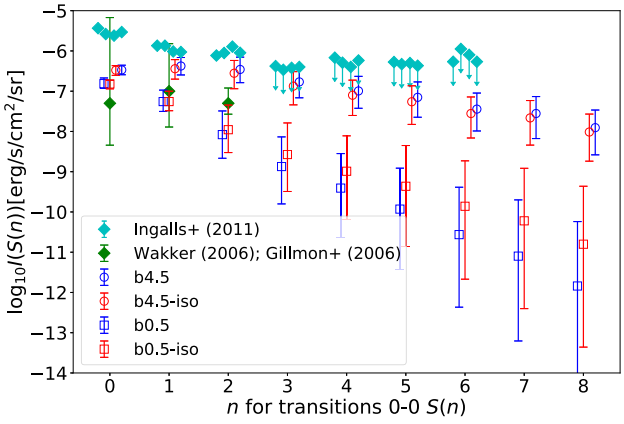

Figure 13. The intensity of each of eight rotational transitions in each of our simulations. The error bars represent 16th and 84th percentiles of the distribution, with the point plotted at the median. The isothermal simulations (after post-processing) look remarkably similar to the non-isothermal simulations. The green points are calculated from *FUSE* observations of AGN behind diffuse H_2 with $10^{19} < N(H_2) < 10^{20}$ cm^{-2} (Gillmon et al. 2006; Wakker 2006); these sightlines have lower N_H than the typical sightlines in our simulations, and are thus expected to differ in intensity by a factor of a few from our simulations. Additional excitation mechanisms appear to be needed to explain the high intensities observed by Ingalls et al. (2011) for the translucent cloud DCld300.2-16.9, and perhaps also the FUSE observations, being lower column density.

of the first three rotational lines $0-0\ S(0)$, $0-0\ S(1)$, and $0-0\ S(2)$. We call this quantity $I(H_2)$. These first three lines contain most of the emission from H_2, and so reflect dissipation into H_2.

Observations of $I(H_2)$ plotted in Fig. 10 are computed using known transition rates from the $v=0, J=2, 3, 4$ levels of H_2 into the $v=0, J=0, 1, 2$ levels, respectively (Wolniewicz, Simbotin & Dalgarno 1998) together with reported J-level column densities.

For all but one of the points, errors are computed from the errors on the column densities in the source literature. For the one point that is not, the column density for $J=4$ was unavailable. To compute upper and lower bounds on the point, we thus see what the greatest ratio of $N(J=4)/N(J=3)$ is across the observations to compute an upper bound on $N(J=4)$, and similarly to compute a lower bound. We take the (logarithmic) mid-point between the upper and lower bounds to be our value for $N(J=4)$ and compute $S(2)$ from this.

All of our simulations exhibit a correlation between N_{CH^+} and $I(H_2)$, as is shown in Fig. 10. In our high field strength simulations, b4.5 and b4.5-iso, there is a relatively strong correlation between $I(H_2)$ and N_{CH^+}, with only $\approx$1 dex of scatter in $\log_{10} N_{CH^+}$ for any given $\log_{10} I(H_2)$. However, at low field strengths, as in b0.5 and b0.5-iso, this correlation is only apparent at higher values of $I(H_2)$, with the correlation disappearing when $I(H_2) \lesssim$ a few $\times\ 10^{-8}\ erg\ s^{-1}\ sr^{-1}\ cm^{-2}$. As the velocity dispersions σ_{3D} are similar across both field strengths, the explanation for the difference between the joint N_{CH^+} versus $I(H_2)$ histograms must lie in their differing ion–neutral drift velocity distributions.

In Fig. 10, we also plot six lines of sight towards various stars, with CH^+ column densities from Lambert & Danks (1986) and $I(H_2)$ computed using column densities of the $v=0, J=2, 3, 4$ states of H_2 published in Spitzer et al. (1974) and Frisch & Jura (1980). These observations agree much better with our simulation data than those from Ingalls et al. (2011). It may be that the Ingalls et al. (2011) cloud is in some way atypical compared to these other simulations.

The higher ion–neutral drift velocities present in our simulations b4.5 and b4.5-iso produce higher values of T_{+AD} compared to our low field strength simulations. Higher values of T_{+AD} mean higher values of $I(H_2)$. Higher values of T_{+AD} also mean higher values of CH^+, but as we stated, the drift velocity dependent component of T_{eff} is much more important to CH^+ than T_{+AD}.

6.5 Polarization and the Stokes parameters, Q and U

To compute the polarization of starlight and thermal emission due to dust grains along a particular line of sight, we compute dimensionless quantities $\tilde{Q}$, $\tilde{U}$, and $\tilde{P}$

$$\tilde{Q}_z = \frac{\int \mathrm{d}z\, \rho (B_y^2 - B_x^2)/B^2}{\int \mathrm{d}z\, \rho} \tag{30}$$

$$\tilde{U}_z = -2\frac{\int \mathrm{d}z\, \rho B_y B_x/B^2}{\int \mathrm{d}z\, \rho} \tag{31}$$

$$\tilde{P}_z = \sqrt{\tilde{U}_z^2 + \tilde{Q}_z^2}, \tag{32}$$

where B_α denotes the component of the magnetic field along direction α, and subscripts on each of the $\tilde{Q}$, $\tilde{U}$, and $\tilde{P}$ denote the axis along which we integrate. The mean field direction is along x, so the above represent sightlines *perpendicular to* the mean field. When computing these parameters along the mean field direction, we simply take $(x, y, z) \rightarrow (y, z, x)$.

Starlight from a star behind the cloud would have fractional Stokes parameters

$$(q_\star, u_\star) = N_\mathrm{d} C_{\mathrm{pol},\star} f_\mathrm{align} \times (\tilde{Q}_z, \tilde{U}_z) \tag{33}$$

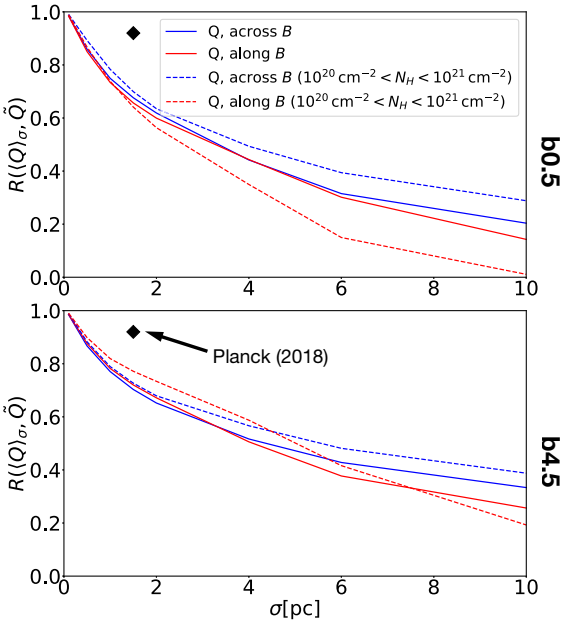

Figure 14. The Pearson correlation coefficient R between $\langle Q\rangle_\sigma$ and $\tilde{Q}$ versus σ for our simulation b0.5 (top) and b4.5 (bottom) (See Tab. 2). We show these values computed both across (blue) and along (red) the mean field direction. Red and blue dashed lines represent the correlation coefficient when computed over a restricted range of column densities ($N_\mathrm{H} \in [10^{20}, 10^{21}]\,\mathrm{cm}^{-2}$) that are more similar to the Planck Collaboration et al. () results. We also show the Planck results for a 40 arcmin beam if the cloud were anywhere between 300 pc away (diamond), where they found $R(\langle Q\rangle_\sigma, Q^*) \approx 0.92$ over a wide range of beam sizes and distances. Note that the correlation coefficient decays more quickly for the lower field strength/higher Alfvén Mach number.

and fractional polarization

$$p_\star = \left(q_\star^2 + u_\star^2\right)^{1/2} = N_\mathrm{d} C_{\mathrm{pol},\star} f_\mathrm{align} \times \tilde{P}_z\ , \tag{34}$$

where $C_{\mathrm{pol},\star}$ is a starlight polarization cross-section, and f_align measures the degree of alignment of dust grains with the local magnetic field (see Appendix C).

For thermal emission, the Stokes parameters Q and U, and the polarized intensity P, are directly related to $\tilde{Q}$, $\tilde{U}$, and $\tilde{P}$, but must also be averaged over a beam (see Appendix C)

$$(\langle Q\rangle_\sigma, \langle U\rangle_\sigma) = B_\nu(T_\mathrm{d}) C_\mathrm{pol} f_\mathrm{align} \times (\langle N_\mathrm{d}\tilde{Q}\rangle_\sigma, \langle N_\mathrm{d}\tilde{U}\rangle_\sigma) \tag{35}$$

$$\langle P\rangle_\sigma = B_\nu(T_\mathrm{d}) C_\mathrm{pol} f_\mathrm{align} \times \left(\langle N_\mathrm{d}\tilde{Q}\rangle_\sigma^2 + \langle N_\mathrm{d}\tilde{U}\rangle_\sigma^2\right)^{1/2}\ , \tag{36}$$

where $\langle ...\rangle_\sigma$ denotes an average over a beam with beam size parameter σ, and $B_\nu(T_\mathrm{d})$ is the blackbody spectrum of a dust grain at temperature T_d. The fractional polarization is (see Appendix C)

$$p_\sigma \approx \frac{C_\mathrm{pol}}{\bar{C}} f_\mathrm{align} \frac{\left(\langle N_\mathrm{d}\tilde{Q}\rangle_\sigma^2 + \langle N_\mathrm{d}\tilde{U}\rangle_\sigma^2\right)^{1/2}}{\langle N_\mathrm{d}\rangle_\sigma}\ . \tag{37}$$

Planck Collaboration XII (2020) find that $(\langle Q\rangle_\sigma, \langle U\rangle_\sigma)$, and $(q_\star, u_\star)$ are highly correlated, with Pearson correlation coefficient 0.92 for a beam with full width at half-maximum (FWHM) = 40 arcmin. Planck Collaboration XII (2020) also find that the ratio $\langle P\rangle_\sigma/p_\star$ changes minimally when the beam size is varied from 20 to 80 arcmin.

Fig. 14 shows the Pearson correlation coefficient R between the beam-averaged $\langle Q\rangle_\sigma$ and the line-of-sight polarization parameter $\tilde{Q}$, as a function of Gaussian beamsize

$$\sigma = \frac{\mathrm{FWHM}}{\sqrt{8\ln 2}} = 1.48\,\mathrm{pc}\left(\frac{\mathrm{FWHM}}{40\,\mathrm{arcmin}}\right)\left(\frac{D}{300\,\mathrm{pc}}\right)\ , \tag{38}$$

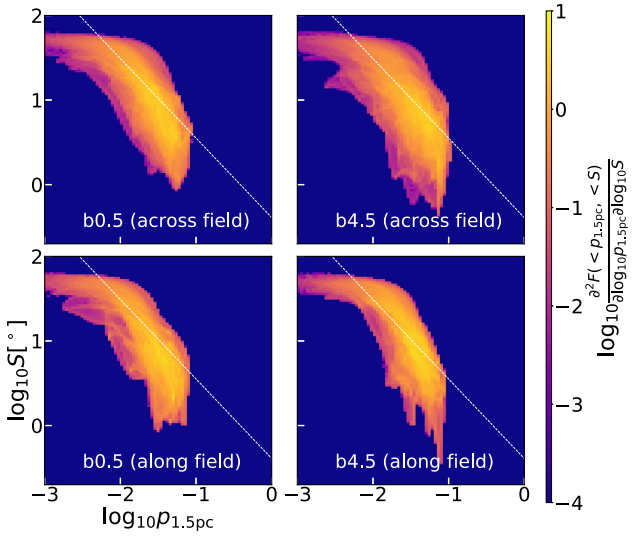

Figure 15. The polarization angle dispersion function S (defined in Section 6.5) versus the polarization p averaged over a Gaussian beam of FWHM = (1.5 pc) × 8ln 2 (see equation B14) for each of our simulations b0.5 and b4.5 (see Tab. 2), computed both across the mean field (top) and along it (bottom). We compute S using an annulus of radius of 0.75 pc and a width of 0.75 pc. Planck Collaboration XX (2015b) found that (approximately) $\log_{10}S[^\circ] = -0.94\log_{10}p - 0.39$ for polarization p over the Chamaeleon–Musca field (other fields are similar). We find that this relationship (white, dashed) is similar to the one our data exhibits.

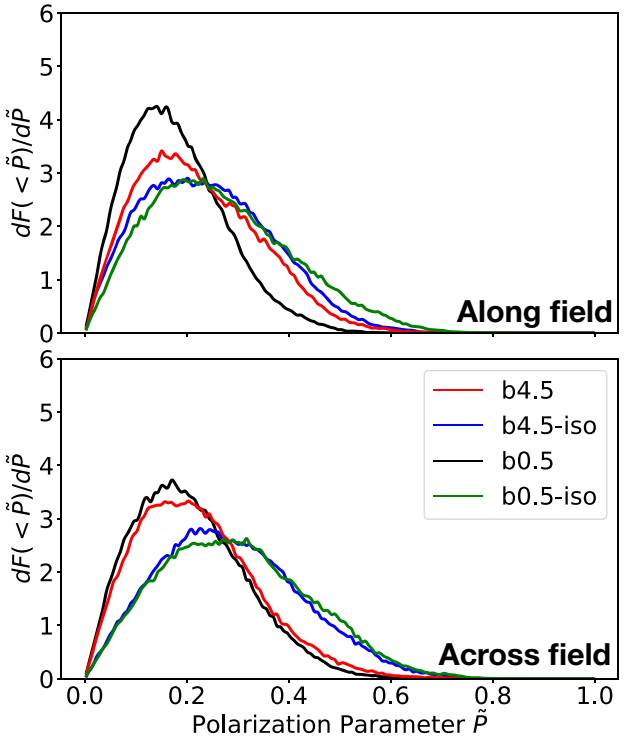

Figure 16. The probability density functions of $\tilde{P}$ in our simulations. As would be expected, across the field, the higher magnetic field, lower Alfvén Mach number simulations have a higher degree of polarization. Viewed along the field, a pattern is less apparent.

for our b4.5 simulation. The correlation is shown for random sightlines along the mean field $\hat{\boldsymbol{x}}B_0$, and across $\hat{\boldsymbol{x}}B_0$. We see that for this simulation, R drops below 0.9 for $\sigma > 0.5$ pc. This contrasts with observations showing $R = 0.92$ for $\sigma \approx 1.5$ pc (for a typical distance $D \approx 300$ pc to the emitting dust).

In order to study the coherence of the polarization in our simulations, we examine at the polarization angle dispersion function S defined by

$$S(\boldsymbol{r}) \equiv \sqrt{\frac{1}{N}\sum_{i=1}^{N}[\psi(\boldsymbol{r}) - \psi(\boldsymbol{r}+\boldsymbol{\delta}_i)]^2} \tag{39}$$

where the sum runs over all lines of sight in an annulus of radius and width 0.75 pc centred around a position $\boldsymbol{r}$, $\psi(\boldsymbol{r})$ is the polarization angle at $\boldsymbol{r}$, and $\boldsymbol{\delta}_i$ is an offset that puts $\boldsymbol{r}+\boldsymbol{\delta}_i$ in the aforementioned annulus (Planck Collaboration XIX 2015a). This corresponds roughly to the parameters that Planck Collaboration XIX (2015a) used for this function given a beam FWHM of 60 arcmin and an annular radius and width of 30 arcmin if we place our simulation at a distance of $D \approx 300$ pc. For consistency, we also use a Gaussian beamsize $\sigma = 1.5$ pc to compute the angles ψ. Fig. 15 shows S versus $p_{1.5\,\mathrm{pc}}$ for our simulations b0.5 and b4.5. To compute this quantity, we have assumed that $C_{\mathrm{pol}}\, f_{\mathrm{align}}/\bar{C} \approx 0.24$. We choose this value because 0.24 is the best estimate for the highest observed level of polarization in Planck Collaboration et al. (). Choosing this value for $C_{\mathrm{pol}}\, f_{\mathrm{align}}/\bar{C}$ ensures that our computed polarizations are always $\leq$0.24.

This function has the property that completely random orientations of the polarization yield $S \approx 52^\circ$, explaining the asymptotic behaviour at low $p_{1.5\,\mathrm{pc}}$ in Fig. 15. Planck Collaboration XIX (2015a) and Planck Collaboration XX (2015b) found an approximate relationship $S \propto 1/p_{1.5\,\mathrm{pc}}$ in both their observational data as well as in a colliding flow MHD simulation. We also find this relationship (shown as a white dashed line in Fig. 15) to approximately hold true for our simulations as well. It is interesting to note that altering the mean field strength/Alfvén Mach number seems to have no effect on this relationship. The relationship also seems unaffected by whether or not we are looking along or across the mean magnetic field direction.

Given that our four simulations differ in one of two ways (either field strength or isothermal/non-isothermal), we may examine the effect that each of those variables has on the polarization. First, does including heating and cooling processes throughout the simulation impact the magnetic field geometry? Fig. 16 shows probability density functions for line-of-sight polarization $\tilde{P}$ in each of our simulations for 512^2 sightlines, both across and along the mean field.

We see no marked difference between polarization in simulations run with an isothermal ($\gamma = 1$) equation of state versus simulations run with $\gamma = 5/3$ and heating (cosmic ray, photoelectric emission from dust grains) and cooling (H_2, C^+, and O) processes included. This suggests that, for the purposes of studying polarization, isothermal MHD turbulence is a reasonable approximation, with heating and cooling processes having only a small effect on the PDFs of dust polarization along lines of sight.

As might have been expected, the higher field strength simulations exhibit higher values of $\tilde{P}$ (see Fig. 16), with the difference being most apparent when looking across the mean field. This makes intuitive sense, as the higher field strength simulations are only moderately super-Alfvénic, with $\mathcal{M}_A \gtrsim 1$. The magnetic field in those simulations is thus moderately effective at resisting distortions due to the turbulent motions in the cloud.

When looking down the field, the polarization we see in all simulations will be due only to a random component of the magnetic field. As a result, we do not expect to see polarization levels quite as

high looking along the mean field as looking across the field, or do we expect as large a difference between the polarization levels for different magnetic field strengths. Indeed, this is what we observe in Fig. 16.

7 DISCUSSION

In our simulations, turbulence and the ambipolar diffusion heating that results from it raise the gas temperature in low density regions to beyond 1000 K, sufficient to produce CH^+. High ion–neutral drift velocities (equation 4) also enhance the CH^+ abundance through increasing the effective reaction temperature (equation 22, see also Fig. 6). As ion–neutral drift velocities are highest in low-density regions, the CH^+ exists predominantly in regions with $n_H \sim 1\,cm^{-3}$. In some fraction of the volume, these drift velocities exceed $5\,km\,s^{-1}$, and so have an ambipolar diffusion Reynolds number $R_{AD} \lesssim 1$. As ambipolar diffusion is important to the dynamics in those regions but we have not properly included it in the dynamics, we have excluded these regions when calculating CH^+ formation and H_2 line emission in our models. This is an important caveat of our results, as the details of these regions could be very important to both the CH^+ abundance and the H_2 rotational line emission (see Fig. 2).

Our simulations include sightlines where $N_H \lesssim 10^{21}$ and $N_{CH^+} \gtrsim 10^{13}\,cm^{-2}$ (see Fig. 9 such sightlines are not seen in the data e.g. Weselak et al. 2008). Because our simulations do not include formation/destruction of H_2, even low column density regions are assumed to have a relatively high H_2 fraction, and thus are able to form CH^+ in our simulation. In reality, photodissociation will suppress the H_2 fraction in low column density regions, where self-shielding is ineffective. Proper treatment of the variable H_2 fraction requires radiative transfer including H_2 self-shielding (V17).

The CH^+ column densities found in MML15 lie between the results of our lowest (b0.5 and b0.5-iso) and highest (b4.5 and b4.5-iso) magnetic field strength simulations. In this way, our results are consistent with theirs. We find that ambipolar diffusion can become a significant factor contributing to the heating of the volume, and cannot be neglected energetically. MML15 found that the contribution to the CH^+ abundance from the ion–neutral drift velocities to be the dominant effect responsible for producing CH^+; we corroborate this finding. The fact that CH^+ is predominantly produced by the ion–neutral drift velocities in our model as well as in the MML15 model is the reason that our results qualitatively agree despite the large discrepancy in our H_2 cooling functions. Both our paper and theirs rely on the same post-processing method to deduce the ion–neutral drift velocities.

As mentioned in Section 1, V17's two-phase, colliding flow results contrast with our findings and those of MML15. V17 found that CH^+ was *not* primarily produced by high ion–neutral drift velocities in their simulation. As well, their simulation underproduced CH^+ relative to observations, finding column densities $\sim 10^{11-12}\,cm^{-2}$ rather than $\sim 10^{13}\,cm^{-2}$. The reasons for this appear to be three-fold. First, destruction of H_2 in low-density regions limits CH^+ production by reaction (1). Secondly, a higher ionization fraction means that ion–neutral drift velocities will be lower, and as we find CH^+ is very sensitive to changes in the ion–neutral drift velocity, this can have an enormous impact on the overall CH^+ abundance. V17 found overall drift velocities around two orders of magnitude lower than those we find. Third, injecting only warm-phase ISM into the box seems likely to underestimate the H_2 fraction in the lower density regions, further decreasing CH^+ abundance.

We suspect there are also key differences in the way the problem is set up in our simulations versus those of V17. V17 used a 2.5 μG guide field aligned with the direction of their flow. We expect this configuration would naturally lead to less tangling of the field in much of the simulation, in particular in the low-density regions where CH^+ is likely produced. In contrast, we used a stronger 4.5 μG mean field and drove turbulence isotropically. It is hard to directly compare our results with theirs given the lack of information on their rms magnetic field strength, Alfvén Mach number, and velocity dispersion in the CNM phase. It seems guaranteed that a colliding flow simulation of this type would produce results differing from those of a simulation of driven turbulence. It would be interesting to know how well a simulation of the V17 type compares to observations of polarization with the same metrics we have used. To understand this problem, multiphase simulations with realistic driving analogous to stellar winds and supernovae are needed.

Of course, both colliding flow simulations and driven turbulence are artificial in their own ways, and likely to produce discrepant results. It is clear that the main difference between our results and those of V17 is the ion–neutral drift velocity. It is essential that future work accurately capture this physics, or at least explore its effect realistically. The biphasic nature of their simulation also impacts the drift velocity distribution. It would be informative in future work to do a multiphase study with H_2 formation and destruction as in V17, but using higher rms magnetic field strengths and a periodic domain driven at large scales the way we have in our study. Recently, Körtgen (2020) showed that turbulence driving in disc galaxies is neither purely compressive nor purely solenoidal. Future simulations may employ driving of this type instead of purely solenoidal driving as we have done.

Our simulations with $B_0 = 4.5$ μG produce rotationally excited H_2 at levels approximately consistent with UV absorption measurements of rotationally excited H_2, and the observed correlation between CH^+ and rotationally excited H_2 is also reproduced (see Figs 10 and 13). However, our models fall short of the strong infrared emission observed from the quiescent translucent cloud DCld 300.2-16.9 (Ingalls et al. 2011). It appears that some additional process is contributing to the H_2 excitation in this cloud.

Planck observations of polarized emission from dust provide a strong test of MHD simulations. The fact that the polarization of dust emission in our simulations is so effectively destroyed by averaging over beams a few pc in size (Fig. 14) is puzzling when compared to the Planck Collaboration XXII (2015d) data. Perhaps the mean field B_0 should be even stronger than $B_0 = 4.5$ μG, thus lowering the Alfvén number. Or perhaps ambipolar diffusion (or some other field-smoothing mechanism) acts more strongly than we have assumed in our simulations, in which ambipolar diffusion has not been treated self-consistently.

In the future, two-fluid simulations that include ambipolar diffusion, full radiative transfer, variable ionization fraction, and time-dependent chemistry will be necessary to fully disentangle all of the separate variables and fully understand the problems we have addressed in this paper. It may not be feasible to model all of these things at once in a volume similar in size to what we have studied here ($8000\,pc^3$), and realistically, future simulations will likely capture one or several of these effects at once, unless effective sub-grid models can be developed.

8 SUMMARY

We present MHD simulations of diffuse molecular clouds 20 pc in size using two different mean magnetic field strengths (0.5 and 4.5 μG). All simulations have the same 3D velocity dispersion (within 10 per cent) chosen to remain consistent with the linewidth–size

relation for molecular clouds (Solomon et al. 1987). We compare simulations using an isothermal equation of state with non-isothermal simulations including realistic heating and cooling. We calculate H_2 cooling over a range of temperatures, densities, and H_2 fractions, and provide an accurate fitting function for the cooling. The MHD simulations were post-processed in a way similar to MML15 to calculate CH^+ abundances, and H_2 excitation and line emission. We compare these results to observations and find that we can explain the CH^+ abundance (Figs 8 and 9), and rotational excitation of H_2 in many regions (Figs 10 and13). However, we fall short of explaining the strong H_2 rotational line intensities seen from two translucent clouds (Ingalls et al. 2011). The H_2 line emission is correlated with the CH^+ (Fig. 10).

CH^+ appears to be primarily manufactured in low-density regions with high ion–neutral drift velocities. These high ion–neutral drift velocities significantly complicate the interpretation of our results because they can become unphysically large. Because of concern about the realism of the high-drift-velocity regions, we calculate CH^+ production and H_2 line emission only from regions where the drift velocity $v_d < 5\,\mathrm{km\,s^{-1}}$, corresponding to ambipolar diffusion Reynolds number $R_{AD} \lesssim 1$. We examine the effects of this cut-off on total H_2 rotational line emission and CH^+ abundance in Fig. 2.

We also construct synthetic line-of-sight velocity distributions for CH^+ and H_2 molecules (Fig. 12). The CH^+ profiles tend to be broader than the neutral line profiles, especially in simulations with a higher mean magnetic field strength.

We compute the polarization of starlight and thermal emission from dust grains and in our MHD simulations, and compare our results to those of Planck Collaboration XII (2020). The polarization statistics are largely unaffected by which method was used for the hydrodynamics (including heating and cooling processes versus using an isothermal equation of state). The polarization does depend on field strength/Alfvén Mach number, with higher field strength (lower Alfvén Mach number) corresponding to higher levels of polarization (Fig. 16).

We examine the effect of averaging the Stokes Q and U over a Gaussian beam of varying width and find our simulations to be marginally inconsistent with the findings of Planck Collaboration XII (2020).

The correlation between beam-averaged polarization of dust thermal emission and polarization of starlight along a sightline is too low in our simulations. We suspect that this is due to our Alfvén Mach number in our simulations ($\mathcal{M}_A \sim 1.2 - 1.4$) being higher than that in nature (perhaps $\mathcal{M}_A \lesssim 1$) on these scales. We speculate that perhaps field-smoothing by ambipolar diffusion in nature is more effective than in our simulations, which do not treat ambipolar diffusion self-consistently.

We conclude that the Alfvén Mach number in interstellar clouds is likely smaller than in our simulations, likely $\mathcal{M}_A \lesssim 1$. Going beyond the work we have done here will require two-fluid simulations to self-consistently model the effects of ambipolar diffusion in multiphase regions.

ACKNOWLEDGEMENTS

We thank Vincent Guillet, Brandon Hensley, Chang-goo Kim, Matthew Kunz, Chris McKee, Eve Ostriker, and Dan Welty for many valuable discussions. We also thank Ivanna Escala for great advice on data visualization. As well, we thank the anonymous reviewer for a careful reading of our manuscript and many helpful comments. This research was supported in part by NSF grants AST-1408723 and AST-1908123.

KT was supported by the Japan Society for the Promotion of Science (JSPS) KAKENHI Grant Numbers 16H05998, 16K13786, 17KK0091, and 18H05440.

DATA AVAILABILITY

The data presented in this paper was generated on the Princeton computing cluster 'Perseus' and will be made freely available upon request to the corresponding author.

REFERENCES

Abgrall H., Roueff E., 1989, A&AS, 79, 313
Abgrall H., Roueff E., Launay F., Roncin J., Subtil J., 1993a, A&AS, 101, 273
Abgrall H., Roueff E., Launay F., Roncin J., Subtil J., 1993b, A&AS, 101, 323
Balakrishnan N., Vieira M., Babb J. F., Dalgarno A., Forrey R. C., Lepp S., 1999, ApJ, 524, 1122
Barinovs Ğ., van Hemert M. C., 2006, ApJ, 636, 923
Black J., Dalgarno A., 1977, ApJS, 34, 405
Celiberto R. et al., 2017, Atoms, 5, 18
Chaffee F., 1975, ApJ, 199, 379
Chakrabarti K., Mezei J. Z., Motapon O., Faure A., Dulieu O., Hassouni K., Schneider I. F., 2018, J. Phys. B At. Mol. Phys., 51, 104002
Coppola C. M., Lique F., Mazzia F., Esposito F., Kazandjian M. V., 2019, MNRAS, 486, 1590
Crompton R. W., Gibson D. K., McIntosh A. I., 1969, Aust. J. Phys., 22, 715
Douglas A. E., Herzberg G., 1941, ApJ, 94, 381
Dove J. E., Teitelbaum H., 1974, Chem. Phys., 6, 431
Draine B. T., 1980, ApJ, 241, 1021
Draine B. T., 1986a, MNRAS, 220, 133
Draine B. T., 1986b, ApJ, 310, 408
Draine B. T., Bertoldi F., 1996, ApJ, 468, 269
Draine B. T., Katz N., 1986a, ApJ, 306, 655
Draine B. T., Katz N., 1986b, ApJ, 310, 392
Draine B. T., Hensley, Brandon S. 2020, preprint (arXiv:2009.11314)
Duley W., Hartquist T., Sternberg A., Wagenblast R., Williams D., 1992, MNRAS, 255, 463
Elitzur M., Watson W. D., 1978, ApJ, 222, L141
Falgarone E., Puget J.-L., 1995, A&A, 293, 840
Flower D. R., Pineau des Forets G., Hartquist T. W., 1985, MNRAS, 216, 775
Frisch P., 1979, ApJ, 227, 474
Frisch P., 1980, ApJ, 241, 697
Frisch P. C., Jura M., 1980, ApJ, 242, 560
Gerlich D., Disch R., Scherbarth S., 1987, J. Chem. Phys., 87, 350
Gillmon K., Shull J. M., Tumlinson J., Danforth C., 2006, ApJ, 636, 891
Glassgold A. E., Galli D., Padovani M., 2012, ApJ, 756, 157
Gry C., Boulanger F., Nehmé C., Pineau des Forêts G., Habart E., Falgarone E., 2002, A&A, 391, 675
Habing H. J., 1968, Bull. Astron. Inst. Neth., 19, 421
Hobbs L., 1973, ApJ, 181, 79
Indriolo N., McCall B. J., 2012, ApJ, 745, 91
Ingalls J. G., Bania T. M., Boulanger F., Draine B. T., Falgarone E., Hily-Blant P., 2011, ApJ, 743, 174
Körtgen B., 2020, MNRAS, 497, 1263
Lacour S., Ziskin V., Hébrard G., Oliveira C., André M. K., Ferlet R., Vidal-Madjar A., 2005, ApJ, 627, 251
Lambert D. L., Danks A. C., 1986, ApJ, 303, 401
Le Bourlot J., Pineau des Forêts G., Flower D. R., 1999, MNRAS, 305, 802
Li P. S., McKee C. F., Klein R. I., Fisher R. T., 2008, ApJ, 684, 380
Linder F., Schmidt H., 1971, Z. Nat.forsch. A, 26, 1603
Lique F., 2015, MNRAS, 453, 810
Lynn J. W., Parrish I. J., Quataert E., Chandran B. D., 2012, ApJ, 758, 78
Mac Low M.-M., Norman M. L., Konigl A., Wardle M., 1995, ApJ, 442, 726
Mathis J. S., Mezger P. G., Panagia N., 1983, A&A, 128, 212
Myers A. T., McKee C. F., Li P. S., 2015, MNRAS, 453, 2747 (MML15)
Pan K., Federman S., Cunha K., Smith V., Welty D., 2004, ApJS, 151, 313

Pan L., Padoan P., 2009, ApJ, 692, 594
Pineau des Forets G., Flower D. R., Hartquist T. W., Dalgarno A., 1986, MNRAS, 220, 801
Planck Collaboration XIX, 2015a, A&A, 576, A104
Planck Collaboration XX, 2015b, A&A, 576, A105
Planck Collaboration XXI, 2015c, A&A, 576, A106
Planck Collaboration XXII, 2015d, A&A, 576, A107
Planck Collaboration XII 2020, A&A, 641, A12
Snow T., 1976, ApJ, 204, 759
Solomon P. M., Rivolo A. R., Barrett J., Yahil A., 1987, ApJ, 319, 730
Spitzer L., Cochran W. D., Hirshfeld A., 1974, ApJS, 28, 373
Sternberg A., Dalgarno A., 1995, Astrophys. J. Suppl., 99, 565
Turner J., Kirby-Docken K., Dalgarno A., 1977, ApJS, 35, 281
Valdivia V., Godard B., Hennebelle P., Gerin M., Lesaffre P., Le Bourlot J., 2017, A&A, 600, A114 (V17)
van Dishoeck E. F., Black J. H., 1986, ApJS, 62, 109
Wakker B. P., 2006, ApJS, 163, 282
Weselak T., Galazutdinov G., Musaev F., Krełowski J., 2008, A&A, 479, 149
White R. E., 1984, ApJ, 284, 695
Wolfire M. G., McKee C. F., Hollenbach D., Tielens A., 2003, ApJ, 587, 278
Wolniewicz L., Simbotin I., Dalgarno A., 1998, ApJS, 115, 293
Zanchet A., Godard B., Bulut N., Roncero O., Halvick P., Cernicharo J., 2013, ApJ, 766, 80

APPENDIX A: NUMERICAL CONVERGENCE

One result of our study has been that the ion–neutral drift velocity v_d plays a critical role in CH^+ formation and excitation of H_2 rotational line emisssion. Here, we examine the sensitivity of v_d to resolution for our simulations with heating and cooling included throughout and an adiabatic $\gamma = 5/3$. In Fig. A1, we show the probability density functions of the ion–neutral drift velocity at four different resolutions, from 64^3 through 512^3, and at two separate mean magnetic field strengths, 0.5 and 4.5 μG. It is worth noting that the highest end of this distribution will never converge in a turbulent domain without ambipolar diffusion being modelled explicitly. This provides additional reason for us to implement a cut in the ion–neutral drift velocities that we consider in our analysis.

Fig. A2 shows the mean ambipolar diffusion heating $\langle \Gamma_{AD} \rangle$ computed only for cells with ion–neutral drift velocities below 5 km s^{-1}. While our results do seem to have some resolution dependence, we would expect this. Only if we were to introduce an explicit physical dissipation mechanism would we expect a well-converged result.

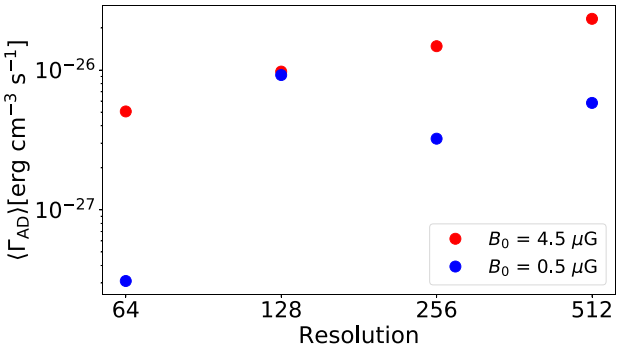

Figure A2. Volume averaged ambipolar diffusion heating calculated for only those regions where the drift velocity $v_d < 5$ km s^{-1}. Points in blue are for the low (0.5 μG) field strength simulations, while points in red are for the high (4.5 μG) field strengths.

APPENDIX B: CALCULATING H_2 LEVEL POPULATIONS AND EMISSION

B1 Radiative processes

We seek to calculate the populations of the (v, J) levels of the H_2 electronic ground state $X^1\Sigma_g^+$. Einstein A coefficients for quadrupole transitions between the different (v, J) levels are taken from Turner, Kirby-Docken & Dalgarno (1977).[3]

Our code allows for photoexcitation out of the ground electronic state to the $B^1\Sigma_u^+$, $C^1\Pi_u^+$, and $C^1\Pi_u^-$ states, followed by either dissociation or return to bound (v, J) levels of the ground electronic state. We use energy levels, Einstein A coefficients, and dissociation probabilities from Abgrall & Roueff (1989) and Abgrall et al.

[3]For all important transitions, these are in agreement with the more recent values from Wolniewicz et al. (1998).

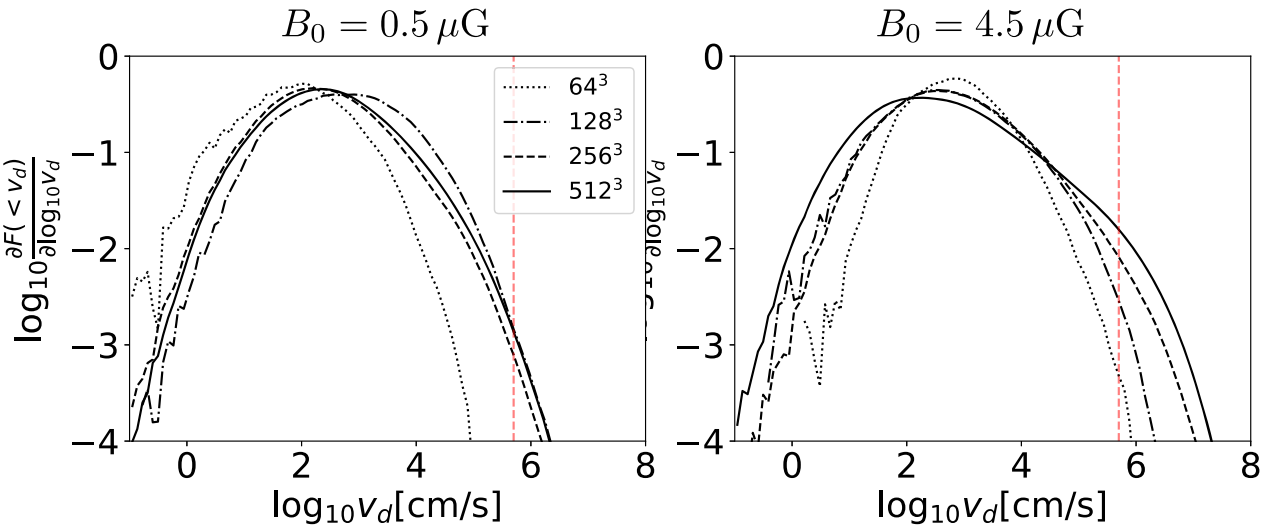

Figure A1. Probability density functions of the ion–neutral drift velocity at various resolutions for each of our chosen mean field strengths, 0.5 and 4.5 μG. The vertical dashed red line represents our 5 km s^{-1} cut that we employ throughout the paper. While it does not appear that our results fully converge, we would not necessarily expect them to: turbulence is an inherently unresolved problem in the absence of physical dissipation.

(1993a,b). However, the results presented here assume ultraviolet pumping to be weak enough so that H_2 excitation is dominated by collisional processes.

B2 Collisional rate coefficients

We include the effects of collisions with H, He, e^-, and H_2 on the rovibrational excitation and deexcitation of H_2. Excitation rates are obtained from deexcitation rates using detailed balance

$$k_{\ell\rightarrow u} = \frac{g_n(J_u)}{g_n(J_\ell)}\left(\frac{2J_u+1}{2J_\ell+1}\right) e^{-(E_u-E_\ell)/kT}\, k_{u\rightarrow\ell}\ , \tag{B1}$$

where $E_u > E_\ell$, and $g_n(J) = 1, 3$ for $J =$ even, odd.

B3 Statistical equilibrium

Let $n_{\rm H} \equiv n({\rm H}) + 2n(H_2) + n(H^+)$ be the number density of H nucleons. We consider the 299 bound rotation-vibration levels of H_2 with rotational quantum number $J \leq 29$, and assign level index i in order of increasing energy E_i, with $i = 0$ corresponding to ($v = 0$, $J = 0$) and $i = 298$ to ($v = 14$, $J = 3$). Let

$$x_i \equiv \frac{2n(H_2(v_i, J_i))}{n_{\rm H}} \qquad , \qquad i = 0, N-1 \tag{B2}$$

be the fraction of the H nucleons in $H_2(v_i, J_i)$, and let

$$x_N \equiv \frac{n({\rm H})}{n_{\rm H}} \tag{B3}$$

be the fraction of the H nucleons in atomic H. We neglect the small fraction of H in molecules other than H_2. The ionized fraction is then $n(H^+)/n_{\rm H} = 1 - \sum_{j=0}^{N} x_j$.

For $f \neq i$, we define a transition matrix

$$R_{if} = k_{if}^{\rm H} n({\rm H}) + k_{if}^{\rm He} n({\rm He}) + k_{if}^{\rm H_2} n(H_2) + A_{if} + \zeta_{if} + \Phi_{if} \tag{B4}$$

where, for $0 \leq i < N$

$$k_{if}^X = \text{ rate coefficient for } X + {\rm H}(v_i, J_i) \rightarrow X + H_2(v_f, J_f) \text{ for } f < N \tag{B5}$$

$$k_{iN}^X = \text{rate coefficient for } X + {\rm H}(v_i, J_i) \rightarrow X + 2{\rm H}, \tag{B6}$$

$$A_{if} = \text{spontaneous decay rate } (f < i < N), \tag{B7}$$

$$\zeta_{if} = i \rightarrow f \text{ transition rate due to UV pumping }, \quad (i < N, f < N), \tag{B8}$$

$$\zeta_{iN} = \text{photodissociation rate } (H_2(v_i, J_i) + h\nu \rightarrow 2{\rm H}) \tag{B9}$$

$$\Phi_{if} = 0 \text{ for } i < N, \tag{B10}$$

$$\Phi_{Nf} = R_{gr} n_{\rm H} \phi_f \text{ for } f < N\ , \tag{B11}$$

where $R_{gr} n_{\rm H} n({\rm H})$ is the rate per volume of H_2 formation on grains, and ϕ_f is the fraction of newly formed H_2 in rotation-vibration state (v_f, J_f).

For convenience, we define the diagonal elements

$$R_{ii} = -\sum_{f\neq i} R_{if}\ . \tag{B12}$$

Then we have

$$\frac{d}{dt}x_f = \sum_{i=0}^{N} R_{if} x_i \quad for\ f = 0, ..., N\ . \tag{B13}$$

B4 Pseudo-steady state

The true steady state solution with $dx_i/dt = 0$ for $i = 0, ..., N$ is one where H_2 dissociation is balanced by H_2 formation. The time-scale for approaching this steady state, $\tau = (2n_{\rm H}R_{gr} + 2\sum_i \zeta_{iN} x_i)^{-1}$, is generally long compared to the time-scales for redistribution over the vibration-rotation states. In fact, H_2 formation and dissociation will often not be balanced in interstellar molecular gas, particularly hot gas that may be cooling rapidly after being shock heated.

Collisional deexcitation of levels that have been populated by UV pumping and injection of newly formed H_2 in excited states can act as a heat source, confusing the calculation of collisional cooling. To remove the effects of UV pumping and isolate the collisional cooling, we treat the atomic fraction $x_N \equiv n({\rm H})/n_{\rm H}$ as a parameter, artificially suppress the rate of H_2 formation by a factor $\lambda_{\rm form} \ll 1$, and find the solution to the set of equations

$$0 = \sum_{i=0}^{N} R'_{if} x_i \quad for\ f = 0, ..., N\ , \tag{B14}$$

where

$$R'_{if} = k_{if}^{\rm H} n({\rm H}) + k_{if}^{\rm H_2} n(H_2) + k_{if}^{\rm He} n({\rm He}) + A_{if} + \lambda_{\rm uv}\zeta_{if} \quad \text{for } i \neq f\ ,\ i < N\ ,\ f < N \tag{B15}$$

$$R'_{iN} = \lambda_{\rm uv}\left[k_{iN}^{\rm H} n({\rm H}) + k_{iN}^{\rm He} n({\rm He}) + k_{iN}^{\rm H_2} n(H_2) + \zeta_{iN}\right]\ , \quad \text{for } i < N \tag{B16}$$

$$R'_{Ni} \equiv \lambda_{\rm form} R_{gr} n_{\rm H} \phi_i \quad \text{for } i < N \tag{B17}$$

$$R'_{ii} \equiv -\sum_{f\neq i} R'_{if}\ , \tag{B18}$$

where the factor $\lambda_{\rm uv}$ modifies all of the dissociation rates to ensure that the steady-state solution to (B14) has the desired atomic fraction x_N

$$\lambda_{\rm uv} \equiv \lambda_{\rm form}\frac{2R_{\rm gr} n_{\rm H} x_N}{\sum_{i=0}^{N-1} x_i R_{iN}}\ . \tag{B19}$$

The rates for UV pumping are also suppressed by the factor $\lambda_{\rm uv}$. Because we take $\lambda_{\rm form} \ll 1$, the H_2 level populations are determined only by collisional processes and spontaneous radiative decay.

B5 $H_2(v, J) + {\rm H}$

Lique (2015) has calculated collisional deexcitation rate coefficients for $H_2(v_u, J_u) + {\rm H} \rightarrow H_2(v_\ell, J_\ell) + {\rm H}$ for the 63 rotation-vibration excited states with $E(v_u, J_u)/hc < 15240\,{\rm cm}^{-1}$ ($E/k < 21930\,{\rm K}$), for temperatures $100\,{\rm K} \leq T \leq 5000\,{\rm K}$. This includes levels up to (v, J) = (0, 17), (1,14), (2,11), and (3,8). We use the Lique (2015) deexcitation rates for deexcitation from these levels. For deexcitation from levels $E(v_u, J_u)/hc > 15240\,{\rm cm}^{-1}$, we use the Lique (2015) rates for the same J_u, J_ℓ, and $v_u - v_\ell$ if available; otherwise we use rates for the same Δv and the highest J_u considered by Lique (2015). For $100\,{\rm K} < T < 5000\,{\rm K}$, we interpolate in the rates provided by Lique (2015). For $T < 100\,{\rm K}$ or $T > 5000\,{\rm K}$, we assume the deexcitation rates to scale as $k \propto \sqrt{T}$.

B6 $H_2(v, J) + H_2$

For collisional deexcitation $H_2(v_u, J_u) + H_2 \rightarrow H_2(v_\ell, J_\ell) + H_2$ we assume that one of the colliding H_2 molecules does not change state;

this is clearly incorrect, but a full set of state-to-state rate coefficients for $H_2 + H_2$ collisions is not yet available. We use the inelastic cross-sections calculated by Le Bourlot et al. (1999) increased by a factor of 3 to obtain vibrational relaxations rates in agreement with the experimental results of Dove & Teitelbaum (1974) at $T = 1000$, 2000, and 3000 K.

For $H_2(v_u, J_u) + He \rightarrow H_2(v_\ell, J_\ell) + He$ we use simple analytical fits to the rates calculated by Le Bourlot et al. (1999).

B7 $H_2(v, J) + He$

For collisional deexcitation $H_2(v_u, J_u) + He \rightarrow H_2(v_\ell, J_\ell) + He$, we use the analytical functions provided by Le Bourlot et al. (1999) to fit their quantum-mechanical results. The results of Balakrishnan et al. (1999) appear to be in good agreement with the Le Bourlot et al. (1999) rates for the $|\Delta J| \leq 4$ transitions that dominate the inelastic collisions.

B8 $H_2(v, J) + e^-$

We consider only $\Delta J = 0$ and ± 2.

For $H_2(v_u, J_u) + e^- \rightarrow H_2(v_u, J_u - 2) + e^-$, we use rates obtained from the $J = 0 \rightarrow 2$ experimental data of Crompton, Gibson & McIntosh (1969) and the $J = 1 \rightarrow 3$ data of Linder & Schmidt (1971)

$$k[(v_u, J_u) \rightarrow (v_u, J_u - 2)] = 2.4 \times 10^{-11} \frac{J_u(2J_u - 3)}{2J_u - 1} \frac{(1 + kT/\Delta E)^{3/2}}{1 + 10^{-3} T_3^2} \ \mathrm{cm^3\ s^{-1}} \quad \text{(B20)}$$

For $\Delta v = -1$ we take

$$k[(v_u, J_u) \rightarrow (v_u - 1, J_\ell)] = 1.2 \times 10^{-10} v_u f(J_u, J_\ell) \left(\frac{T_3 + 0.8 T_3^{1.2}}{1 + 0.005 T_3^2} \right) \mathrm{cm^3\ s^{-1}}\ , \quad \text{(B21)}$$

with

$$f(J_u, J_\ell) \equiv \frac{2J_\ell + 1}{4J_u + 6} \quad for\ J_u \leq 1 \quad \text{(B22)}$$

$$\equiv \frac{2J_\ell + 1}{6J_u + 3} \quad for\ J_u \geq 2\ . \quad \text{(B23)}$$

For $\Delta v = -2$ and $\Delta v = -3$ we take

$$k[(v_u, J_u) \rightarrow (v_u - 2, J_\ell)] = 3 \times 10^{-12} v_u f(J_u, J_\ell) \frac{T_3^{1.6}}{1 + 0.003 T_3^2} \ \mathrm{cm^3\ s^{-1}} \quad \text{(B24)}$$

$$k[(v_u, J_u) \rightarrow (v_u - 3, J_\ell)] = 1.2 \times 10^{-12} v_u f(J_u, J_\ell) \frac{T_3^{1.5}}{1 + 0.018 T_3^2} \ \mathrm{cm^3\ s^{-1}}\ . \quad \text{(B25)}$$

For $\Delta v = -4, -5, -6$ we take

$$k[(v_u, J_u) \rightarrow (v_\ell, J_\ell)] = 2 \times 10^{-13} v_u f(J_u, J_\ell) \frac{T_3^{1.5}}{1 + 0.01 T_3^2} \ \mathrm{cm^3\ s^{-1}}$$

APPENDIX C: POLARIZATION BY ALIGNED DUST GRAINS

Suppose the dust grains to be oblate spheroids, with cross-sections C_a and C_b for **E** parallel and perpendicular to the symmetry axis $\hat{\mathbf{a}}$. Consider directions $\hat{\mathbf{x}}$ and $\hat{\mathbf{y}}$ in the plane of the sky. In the Rayleigh limit $\lambda \gg a_{\rm eff}$, a dust grain will have cross-sections

$$C_x = C_a(\hat{\mathbf{a}} \cdot \hat{\mathbf{x}})^2 + C_b[1 - (\hat{\mathbf{a}} \cdot \hat{\mathbf{x}})^2] \quad \text{(C1)}$$

$$C_y = C_a(\hat{\mathbf{a}} \cdot \hat{\mathbf{y}})^2 + C_b[1 - (\hat{\mathbf{a}} \cdot \hat{\mathbf{y}})^2] \quad \text{(C2)}$$

for radiation with **E** in the $\hat{\mathbf{x}}$ and $\hat{\mathbf{y}}$ directions, respectively. Let $f_{\rm align}$ measure the alignment of grain axes $\hat{\mathbf{a}}$ with the local magnetic field direction $\hat{\mathbf{b}} \equiv \mathbf{B}/B$

$$f_{\rm align} \equiv \frac{3}{2} \left[\langle (\hat{\mathbf{a}} \cdot \hat{\mathbf{b}})^2 \rangle - \frac{1}{3} \right]\ . \quad \text{(C3)}$$

Randomly oriented grains have $\langle (\hat{\mathbf{a}} \cdot \hat{\mathbf{b}})^2 \rangle = 1/3$ and $f_{\rm align} = 0$; perfectly oriented grains have $f_{\rm align} = 1$. We assume $f_{\rm align}$ to be independent of position. Define

$$\beta_x(x, y) \equiv \frac{\int dz\, \rho\, (\hat{\mathbf{b}} \cdot \hat{\mathbf{x}})^2}{\int dz\, \rho} \quad \text{(C4)}$$

$$\beta_y(x, y) \equiv \frac{\int dz\, \rho\, (\hat{\mathbf{b}} \cdot \hat{\mathbf{y}})^2}{\int dz\, \rho} \quad \text{(C5)}$$

$$\beta_{xy}(x, y) \equiv 2 \frac{\int dz\, \rho\, (\hat{\mathbf{b}} \cdot \hat{\mathbf{x}})(\hat{\mathbf{b}} \cdot \hat{\mathbf{y}})}{\int dz\, \rho} \quad \text{(C6)}$$

$$\tilde{Q}(x, y) \equiv \beta_x - \beta_y \quad \text{(C7)}$$

$$\tilde{U}(x, y) \equiv -\beta_{xy} \quad \text{(C8)}$$

$$\tilde{P}(x, y) \equiv \left(\tilde{Q}^2 + \tilde{U}^2 \right)^{1/2}\ . \quad \text{(C9)}$$

Suppose the grains have $\hat{\mathbf{a}} \cdot \hat{\mathbf{b}} = \cos\theta$, with $\hat{\mathbf{a}}$ precessing around $\hat{\mathbf{b}}$. Averaging over the precession and along the sightline

$$\langle (\hat{\mathbf{a}} \cdot \hat{\mathbf{x}})^2 \rangle = f_{\rm align} \beta_x + \frac{1}{3} \left(1 - f_{\rm align} \right) \quad \text{(C10)}$$

$$\langle (\hat{\mathbf{a}} \cdot \hat{\mathbf{y}})^2 \rangle = f_{\rm align} \beta_y + \frac{1}{3} \left(1 - f_{\rm align} \right)\ . \quad \text{(C11)}$$

Define

$$\bar{C} \equiv \frac{2C_b + C_a}{3} \quad \text{(C12)}$$

$$C_{\rm pol} \equiv \frac{C_b - C_a}{2}\ . \quad \text{(C13)}$$

In the Rayleigh limit, an optically thin sightline has emitted intensity

$$I = \frac{1}{2} N_{\rm d} B_\nu(T_{\rm d}) \left[\langle C_x \rangle + \langle C_y \rangle \right] \quad \text{(C14)}$$

$$= N_{\rm d} B_\nu(T_{\rm d}) \left[\bar{C} + f_{\rm align} C_{\rm pol} \left(\frac{2}{3} - \beta_x - \beta_y \right) \right]\ . \quad \text{(C15)}$$

The Stokes Q and U, and polarized intensity P are

$$Q = \frac{1}{2} N_{\rm d} B_\nu(T_{\rm d}) (\langle C_x \rangle - \langle C_y \rangle) = N_{\rm d} B_\nu(T_{\rm d}) C_{\rm pol} f_{\rm align} (\beta_y - \beta_x) = N_{\rm d} B_\nu(T_{\rm d}) C_{\rm pol} f_{\rm align} \tilde{Q} \quad \text{(C16)}$$

$$U = -N_{\rm d} B_\nu(T_{\rm d}) C_{\rm pol} f_{\rm align} \beta_{xy} = N_{\rm d} B_\nu(T_{\rm d}) C_{\rm pol} f_{\rm align} \tilde{U} \quad \text{(C17)}$$

$$P = (Q^2 + U^2)^{1/2}\ . \quad \text{(C18)}$$

Let $\langle ... \rangle_\sigma$ denote a beam average. The polarized intensity and total intensity are

$$\langle P \rangle_\sigma = B_\nu(T_{\rm d}) C_{\rm pol} f_{\rm align} \left(\langle N_{\rm d} \tilde{Q} \rangle_\sigma^2 + \langle N_{\rm d} \tilde{U} \rangle_\sigma^2 \right)^{1/2} \quad \text{(C19)}$$

$$\langle I\rangle_\sigma = B_\nu(T_\mathrm{d})\bar{C}\langle N_\mathrm{d}\rangle_\sigma \times\left[1+f_\mathrm{align}\frac{C_\mathrm{pol}}{\bar{C}}\left(\frac{2}{3}-\frac{\langle N_\mathrm{d}\beta_x\rangle_\sigma}{\langle N_\mathrm{d}\rangle_\sigma}-\frac{\langle N_\mathrm{d}\beta_y\rangle_\sigma}{\langle N_\mathrm{d}\rangle_\sigma}\right)\right] \approx B_\nu(T_\mathrm{d})\bar{C}\langle N_\mathrm{d}\rangle_\sigma \quad \text{(C20)}$$

The beam-averaged fractional polarization is

$$p=\frac{\langle P\rangle_\sigma}{\langle I\rangle_\sigma}\approx\frac{C_\mathrm{pol}}{\bar{C}}f_\mathrm{align}\frac{\left(\langle N_\mathrm{d}\tilde{Q}\rangle_\sigma^2+\langle N_\mathrm{d}\tilde{U}\rangle_\sigma^2\right)^{1/2}}{\langle N_\mathrm{d}\rangle_\sigma}\ . \quad \text{(C21)}$$

Aligned grains polarize starlight. Let $C_{a,\star}$ and $C_{b,\star}$ be extinction cross-sections for starlight polarized parallel or perpendicular to $\hat{\mathbf{a}}$. The 'modified picket fence approximation' (MPFA) consists of using equations (C1) and (C2) even at wavelengths that are comparable to the grain size. Draine & Hensley (2020) show that the MPFA is sufficiently accurate to use in modeling starlight polarization. The difference in extinction cross-section for radiation polarized perpendicular or parallel to the projection of $\mathbf{B}$ on the plane of the sky is then

$$C_{\mathrm{ext}\star,\parallel}-C_{\mathrm{ext}\star,\perp}=\left[C_{b,\star}-C_{a,\star}\right]f_\mathrm{align}[(\hat{\mathbf{b}}\cdot\hat{\mathbf{x}})^2+(\hat{\mathbf{b}}\cdot\hat{\mathbf{y}})^2] \quad \text{(C22)}$$

and initially unpolarized radiation develops a polarization characterized by

$$(q_\star,u_\star)\approx N_d C_{\mathrm{pol}\star}f_\mathrm{align}(\tilde{Q},\tilde{U}) \quad \text{(C23)}$$

$$C_{pol,\star}\equiv\frac{C_{b,\star}-C_{a,\star}}{2}\ . \quad \text{(C24)}$$

The fractional polarization of the starlight is

$$p_\star=\left(q_\star^2+u_\star^2\right)^{1/2}\ . \quad \text{(C25)}$$

This paper has been typeset from a TEX/LATEX file prepared by the author.